### **OPEN ACCESS**



# Near-infrared Supernova Ia Distances: Host Galaxy Extinction and Mass-step Corrections Revisited

J. Johansson<sup>1</sup>, S. B. Cenko<sup>2,3</sup>, O. D. Fox<sup>4</sup>, S. Dhawan<sup>1</sup>, A. Goobar<sup>1</sup>, V. Stanishev<sup>5</sup>, N. Butler<sup>6</sup>, W. H. Lee<sup>7</sup>, A. M. Watson<sup>7</sup>, U. C. Fremling<sup>8</sup>, M. M. Kasliwal<sup>8</sup>, P. E. Nugent<sup>9,10</sup>, T. Petrushevska<sup>11</sup>, J. Sollerman<sup>12</sup>, L. Yan<sup>13</sup>, J. Burke<sup>14,15</sup>, G. Hosseinzadeh<sup>16</sup>, D. A. Howell<sup>14,15</sup>, C. McCully<sup>14,15</sup>, and S. Valenti<sup>17</sup> Astrophysics Science Division, NASA Goddard Space Flight Center, Mail Code 661, Greenbelt, MD 20771, USA Joint Space-Science Institute, University of Maryland, College Park, MD 20742, USA Space Telescope Science Institute, 3700 San Martin Dr, Baltimore, MD 21218 USA <sup>5</sup> Department of Physics, Chemistry and Biology, IFM, Linköping University, SE-58183 Linköping, Sweden School of Earth and Space Exploration, Arizona State University, Tempe, AZ 85287, USA <sup>7</sup> Instituto de Astronomía, Universidad Nacional Autónoma de México, Apartado Postal 70-264, 04510 CDMX, México Division of Physics, Mathematics, and Astronomy, California Institute of Technology, Pasadena, CA 91125, USA Lawrence Berkeley National Laboratory, 1 Cyclotron Rd, Berkeley, CA 94720, USA Department of Astronomy, University of California, Berkeley, Berkeley, CA 94720, USA <sup>11</sup> Centre for Astrophysics and Cosmology, University of Nova Gorica, Vipavska 11c, 5270 Ajdovščina, Slovenia <sup>12</sup> The Oskar Klein Centre, Department of Astronomy, Stockholm University, AlbaNova, SE-10691 Stockholm, Sweden Caltech Optical Observatories, California Institute of Technology, Pasadena, CA 91125, USA Department of Physics, University of California, Santa Barbara, CA 93106-9530, USA 15 Las Cumbres Observatory, 6740 Cortona Dr, Suite 102, Goleta, CA 93117-5575, USA <sup>16</sup> Center for Astrophysics | Harvard & Smithsonian, 60 Garden St, Cambridge, MA 02138-1516, USA Department of Physics and Astronomy, University of California, 1 Shields Ave, Davis, CA 95616-5270, USA Received 2021 May 24; revised 2021 October 11; accepted 2021 October 12; published 2021 December 24

### **Abstract**

We present optical and near-infrared (NIR, Y-, J-, H-band) observations of 42 Type Ia supernovae (SNe Ia) discovered by the untargeted intermediate Palomar Transient Factory survey. This new data set covers a broad range of redshifts and host galaxy stellar masses, compared to previous SN Ia efforts in the NIR. We construct a sample, using also literature data at optical and NIR wavelengths, to examine claimed correlations between the host stellar masses and the Hubble diagram residuals. The SN magnitudes are corrected for host galaxy extinction using either a global total-to-selective extinction ratio,  $R_V = 2.0$ , for all SNe, or a best-fit  $R_V$  for each SN individually. Unlike previous studies that were based on a narrower range in host stellar mass, we do not find evidence for a "mass step," between the color- and stretch-corrected peak J and H magnitudes for galaxies below and above  $\log(M_*/M_\odot) = 10$ . However, the mass step remains significant  $(3\sigma)$  at optical wavelengths (g, r, i) when using a global  $R_V$ , but vanishes when each SN is corrected using their individual best-fit  $R_V$ . Our study confirms the benefits of the NIR SN Ia distance estimates, as these are largely exempted from the empirical corrections dominating the systematic uncertainties in the optical.

Unified Astronomy Thesaurus concepts: Type Ia supernovae (1728); Cosmology (343); Interstellar dust extinction (837)

Supporting material: machine-readable table

#### 1. Introduction

Since the initial standardization of Type Ia supernova (SN Ia) peak luminosities was employed in the discovery of the accelerated expansion of the universe (Riess et al. 1998; Perlmutter et al. 1999), estimates of the local value of the Hubble constant from SNe ( $H_0$ ; Riess et al. 2019) are in tension with the value inferred from the early universe (Planck Collaboration et al. 2020). This tension is a possible sign of new physics or unresolved sources of systematic uncertainty.

Significant work has gone into understanding how to more precisely standardize SNe Ia as distance indicators at optical (visible) wavelengths. The SN Ia optical peak brightness is corrected for lightcurve shape (Phillips 1993) and color (Tripp 1998), and there are now several more elaborated prescriptions for

Original content from this work may be used under the terms of the Creative Commons Attribution 4.0 licence. Any further distribution of this work must maintain attribution to the author(s) and the title of the work, journal citation and DOI.

optimizing these standardization procedures (see, e.g., Guy et al. 2007; Burns et al. 2011; Mandel et al. 2011). More recently, additional correction terms aiming at further improving the SN Ia standard candle have also been proposed. One such term accounts for the dependence of the SN Ia luminosity on its host galaxy properties, e.g., stellar mass (Hamuy et al. 1995; Sullivan et al. 2003; Lampeitl et al. 2010; Childress et al. 2013; Betoule et al. 2014; Uddin et al. 2017; Scolnic et al. 2018; Wiseman et al. 2020; Kelsey et al. 2021). These studies all uncover, to various degrees of significance, a "mass step" in the data: after lightcurve standardization, SNe in high-mass galaxies are more luminous than those exploding in low-mass galaxies. The origin of this mass step is poorly understood. Possible explanations include intrinsic differences in the SN populations and extrinsic differences in the host galaxy dust properties (Brout & Scolnic 2021). Near-infrared (NIR;  $1 < \lambda < 2.5 \mu m$ ) observations offer many advantages for standardizing SNe Ia (Elias et al. 1985; Meikle 2000) and for testing the hypothesis of different host galaxy dust properties. SNe Ia are more naturally standard candles at these wavelengths,

requiring significantly smaller corrections to their peak luminosity to yield similar precision as compared to the optical (Krisciunas et al. 2004; Wood-Vasey et al. 2008; Mandel et al. 2009; Burns et al. 2011, 2018; Dhawan et al. 2018a; Avelino et al. 2019). The reported scatter in NIR absolute magnitudes of  $\lesssim$ 0.15 mag is also supported by theoretical models, which indicate small variations of <0.1–0.2 mag in the peak NIR magnitudes despite widely varying physical properties of the ejecta (Kasen 2006; Blondin et al. 2015). Furthermore, the NIR is less affected by dust extinction, e.g., the *J*band extinction is a factor of  $\sim$ 4 lower than in V-band for typical dust. If different dust properties in low- and high-mass host galaxies are the cause of the mass step, the size of the mass step should be wavelength dependent (larger in the optical and smaller in the NIR; see, e.g., Figure 13 in Uddin et al. 2020) There are already upcoming data sets (e.g., CSP-II, Sweetspot, and RAISIN; Phillips et al. 2019; Ponder et al. 2020; Kirshner 2013), and ongoing (e.g., SIRAH, DEHVILS, and VEILS; Jha et al. 2019) and future SN Ia programs (e.g., with the Nancy Grace Roman Space Telescope; Hounsell et al. 2018) aiming to take advantage of these properties of SNe Ia and use NIR observations to study dark energy. In this context, NIR observations of SNe Ia in the nearby Hubble flow ( $z \ge 0.03$ ) are extremely valuable cosmological tools both as a Hubble flow rung of the local distance ladder and as a low-z "anchor" sample to measure dark energy properties.

However, as Burns et al. (2018) point out, there is a deficit of SNe in low-mass hosts in the current SN Ia NIR data set, and observing an unbiased sample of SNe Ia in the nearby Hubble flow is crucial to test the impact of SN Ia systematics, e.g., extinction from host galaxy dust, on the inferred value of  $H_0$  (Burns et al. 2018; Dhawan et al. 2018a). Moreover, recent works have also claimed evidence for a mass step in the NIR as well (Ponder et al. 2020; Uddin et al. 2020). If indeed present and not accounted for, it will introduce further systematic uncertainties in the NIR SN Ia cosmological analyses.

The main goal of this work is to obtain optical and NIR lightcurves of an unbiased sample of SNe Ia in the nearby Hubble flow, together with data from the literature, to examine the impact of the host galaxy extinction determination on the claimed correlations between the host stellar masses and the NIR Hubble diagram residuals.

Here, we present optical and NIR observations of a new sample of 42 SNe Ia with redshifts out to  $z \sim 0.12$  and containing 12 SNe in hosts with masses below  $\log(M_*/M_\odot) = 10$ .

Section 2 presents our sample. Section 3 describes our observations. Section 4 presents our analysis techniques, including spectroscopic classification, lightcurve fitting, derivation of the NIR Hubble diagram, and correlations with the host galaxy stellar mass. Section 5 discusses the results, and Section 6 provides our conclusion.

Throughout this paper we assume a flat  $\Lambda$ CDM cosmological model with  $\Omega_M = 0.27$  and Hubble constant  $H_0 = 73.2 \,\mathrm{km \, s}^{-1} \,\mathrm{Mpc}^{-1}$  from Burns et al. (2018).

### 2. Supernova Sample

This work presents 42 new SNe Ia discovered with the intermediate Palomar Transient Factory (iPTF; Rau et al. 2009). We chose targets spanning a wide range of redshifts and host galaxy environments, and acquired optical and NIR follow-up observations for targets with early iPTF detection and classification. These observations are described in more detail in Section 3.

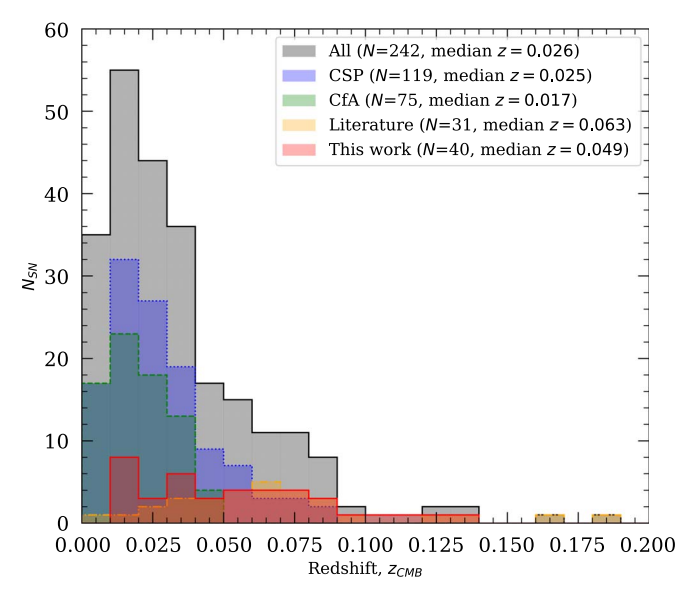


**Figure 1.** Redshift distribution of the SNe used in the analysis. Note that peculiar SNe Ia are not included here, as well as SNe lacking optical lightcurves. The total number of unique SNe with both optical and NIR lightcurves amounts to 242.

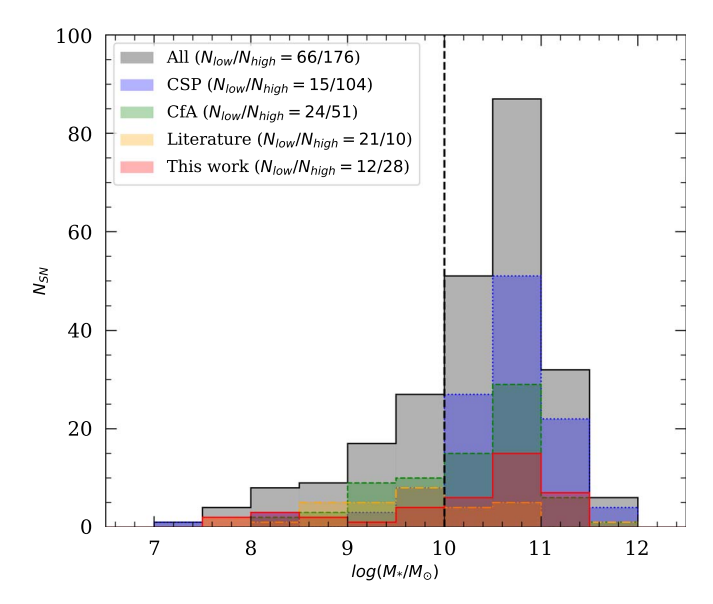


Figure 2. Host galaxy mass distribution of the SNe used in the analysis.

For our analysis, we also include SNe Ia from the literature having both optical and NIR lightcurves, which we describe briefly here and summarize in Figures 1 and 2. The final photometry of the first stage of the Carnegie Supernova Project (CSP-I) are presented in Krisciunas et al. (2017). Their sample consists of 120 SNe with NIR coverage, z = 0.0037-0.0835. CfAIR2 (Friedman et al. 2015) is a sample of NIR lightcurves for 94 SNe Ia obtained with the 1.3 m Peters Automated InfraRed Imaging TELescope (PAIRITEL) between 2005 and 2011. Barone-Nugent et al. (2012) present J- and H-band lightcurves of 12 SNe Ia discovered by PTF in the redshift range 0.03 < z < 0.08. This data was re-analyzed by Stanishev et al. (2018), including optical lightcurves. Stanishev et al. (2018) add 16 more SNe with NIR data in the redshift range z = 0.037-0.183. Furthermore, we include the six SNe with UV, optical, and NIR lightcurves in Amanullah et al. (2015). Note that some of the

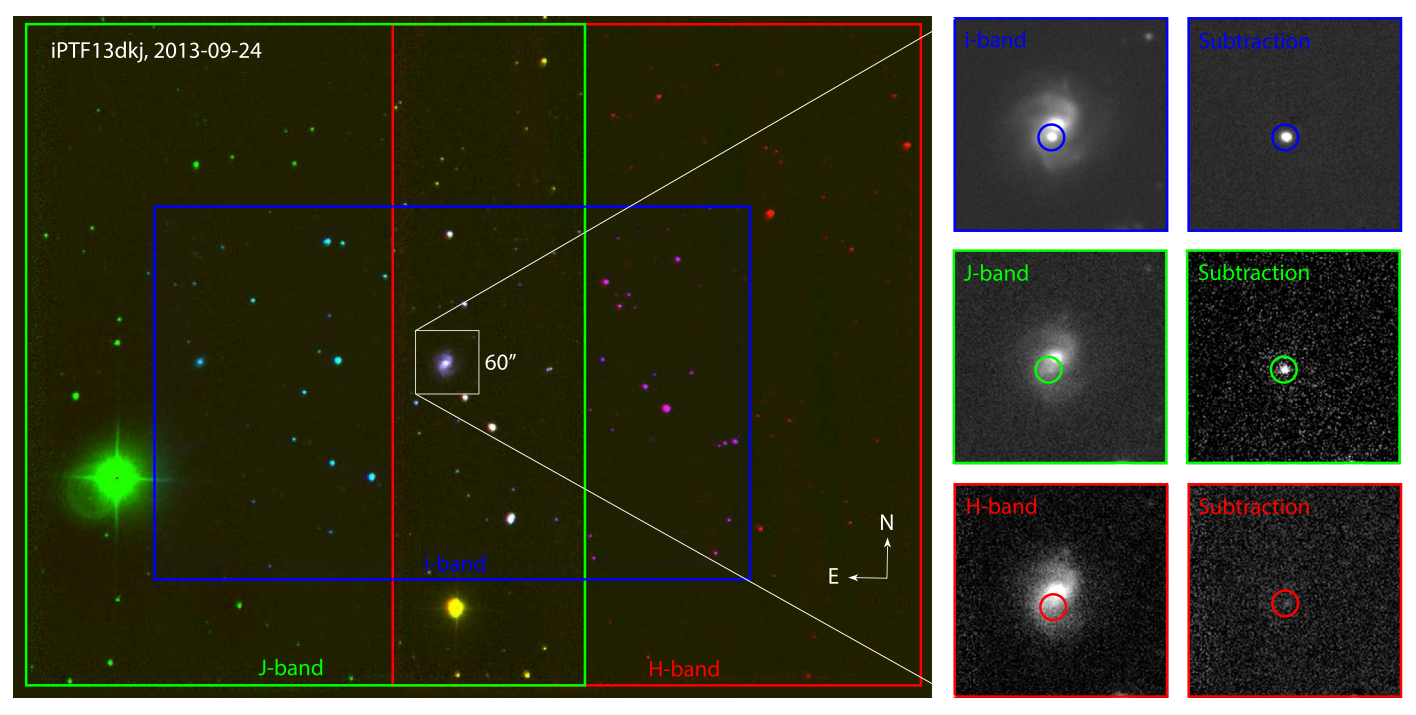


Figure 3. Example of typical RATIR observations for iPTF13dkj (at z = 0.036) from 2013 September 24. For the RGB composite (left panel), the blue, green, and red insets show i-, J-, and H-band images, respectively. The middle and right panels show the  $60'' \times 60''$  region centered on the SN and host galaxy.

supernovae were observed by, e.g., both CSP and CfA (see Friedman et al. 2015, for a comparison), and the total sample size in Figures 1 and 2 refers to the number of unique SNe.

### 3. Observations

The follow-up observations were obtained with several different facilities, which are described in the following sections. For each instrument used, deep reference images were obtained after the supernova emission had faded away. The reference images were subtracted from the science images in order to facilitate the photometry of the SNe, which can otherwise be affected by the light of the host galaxy. Image subtraction was in most cases performed as part of the reduction pipelines, which all utilize implementation of the convolution algorithms presented in Alard & Lupton (1998).

## 3.1. Optical Data

During the intermediate Palomar Transient Factory (iPTF) survey, the Palomar 48 inch (P48) telescope typically delivered *g*- and *R*-band images. The P48 image reduction is described by Laher et al. (2014), while the PTF photometric calibration and the photometric system are discussed by Ofek et al. (2012).

Optical follow-up observations were collected using the Palomar 60 inch telescope (P60, BVgriz filters), the 2.56 m Nordic Optical Telescope (NOT), and the Las Cumbres Observatory (LCO) in UBVRI and/or griz-bands. The P60 data were reduced using an automated pipeline (Cenko et al. 2006), calibrated against the Sloan Digital Sky Survey (SDSS) and the reference images subtracted using FPipe (Fremling et al. 2016). Similarly, the NOT data were reduced with standard IRAF routines using the QUBA pipeline (Valenti et al. 2011), calibrated to the Landolt system through observations of standard stars and SDSS stars in the field. LCO data were reduced using lcogtsnpipe (Valenti et al. 2016) by performing point-spread function (PSF) fitting photometry. Zero-points for images in the

*UBVRI* filters were calculated from Landolt standard fields (Landolt 1992) taken on the same night by the same telescope. For images in the *griz* filter set, zero-points were calculated using SDSS magnitudes of stars in the same field as the object.

### 3.2. Near-infrared Observations

For 37 out of 42 SNe in our sample, we acquired follow-up observations using the Reionization and Transients InfraRed camera (RATIR). RATIR is a six-band simultaneous optical and NIR imager (*riZYJH* bands) mounted on the autonomous 1.5 m Harold L. Johnson Telescope at the Observatorio Astronómico Nacional on Sierra San Pedro Mártir in Baja California, Mexico (Butler et al. 2012; Fox et al. 2012; Klein et al. 2012; Watson et al. 2012).

Typical observations include a series of 80 s exposures in the *ri* bands and 60 s exposures in the *ZY JH* bands, with dithering between exposures. The fixed IR filters of RATIR cover half of their respective detectors, automatically providing off-target IR sky exposures while the target is observed in the neighboring filter. Master IR sky frames are created from a median stack of off-target images in each IR filter. No off-target sky frames were obtained on the optical CCDs, but the small galaxy sizes and sufficient dithering allowed for a sky frame to be created from a median stack of selected images in each filter that did not contain either a bright star or an extended host galaxy.

Flat-field frames consist of evening sky exposures. Given the lack of a cold shutter in RATIR's design, IR dark frames are not available. Laboratory testing, however, confirms that the dark current is negligible in both IR detectors (Fox et al. 2012). Bias subtraction and twilight flat division are performed using algorithms written in PYTHON, image alignment is conducted by astrometry.net (Lang et al. 2010), and image co-addition is achieved using SWARP (Bertin 2010). Figure 3 shows a typical set of images, where blue, green, and red show the field of view for the *i*-, *J*-, and *H*-band frames, respectively.

For seven SNe Ia in our sample, *J*- and *H*-band observations were also obtained using other facilities, such as HAWK-I on the 8 m Very Large Telescope (VLT; for iPTF14bbr, 14ddi, 14deb, 14eje, and 14fww), VIRCAM on the 4 m VISTA telescope (iPTF14fpb), and WIRC on the Palomar 200 inch telescope (iPTF14gnl). These observations were processed with the corresponding instrument reduction pipelines.

### 3.3. Image Subtraction

Image subtraction was performed utilizing the High Order Transform of PSF ANd Template Subtraction (HOTPANTS; Becker 2015). Point sources were selected across the field of view (FOV) to calculate the PSF in each image, either based on classification from SDSS or through manual inspection. Given the relative paucity of bright point sources in most fields (particularly in the NIR), the PSF was held fixed across the FOV.

The calculated PSFs were utilized to perform PSF-matched photometry on the resulting subtracted images, yielding measurements of the instrumental magnitude of the supernovae in each epoch:

$$m_{f,\text{inst}} = -2.5 \log_{10} \frac{\text{ADU}}{t_{\text{exp}}}.$$
 (1)

Uncertainties and upper limits were determined by inserting false sources of varying brightness into the RATIR images and repeating the identical process of image subtraction and PSFmatched photometry.

### 3.4. Photometric Calibration

Photometric calibration of the RATIR data was performed following the process outlined in Ofek et al. (2012). To calculate color and illumination terms, we selected fields with coverage from both SDSS (optical) and UKIDSS (NIR), and obtained photometry for stars (i.e., objects classified as point sources in SDSS) with *r*-band magnitudes between 14 and 18 (with additional flagging for saturation). We measured instrumental magnitudes via PSF-matched photometry for these calibration stars as above.

As a first pass, we calculate a zero-point for each image with no additional corrections (e.g., color and illumination terms). We removed nights with a large scatter in the zero-point (rms  $\geqslant 0.10$  mag) or individual stars that were clear outliers in the fits (determined via visual inspection).

We then perform a least-squares fit using the remaining nights/stars to the following equation for each filter *f*:

$$m_f = m_{f,inst} + ZP + CT_{f,i,j} \cdot (m_i - m_j) + C_{illum}$$
 (2)

where ZP is the zero-point,  $CT_{f,i,j}$  is the color term,  $m_i$  and  $m_j$  are the filters used for the color correction, and  $C_{illum}$  is an illumination correction term accounting for PSF variations depending on the position on the detector.

The color and illumination terms are held fixed for all observations in a given filter, while the zero-point term is allowed to vary freely in each image. The resulting best-fit color terms and zero-point rms are shown in Table 1. The zero-point rms is typically  $\sim 0.03$  mag for the RATIR r to H bands.

For fields with SDSS and UKIDSS coverage, calibrated supernova magnitudes are calculated using Equation (2). For fields lacking SDSS coverage, we use photometry from Pan-STARRS1 Data Release 2 (Magnier et al. 2020), which is in a photometric system close to SDSS (Tonry et al. 2012). For fields lacking UKIDSS coverage we use 2MASS (Skrutskie et al. 2006)

Table 1
RATIR Photometric Calibration

Filter	Color Term $C_{f,ij}$	Color $(i-j)$	ZP rms (mag)	Limiting (mag)
$\overline{r}$	0.009	(r-i)	0.031	21.54
i	0.030	(r-i)	0.025	21.52
Z	-0.048	(i-z)	0.032	20.80
Y	0.046	(Y-J)	0.031	19.81
J	0.057	(J-H)	0.026	18.94
H	-0.054	(J-H)	0.032	18.27

 Table 2

 Photometry for 42 SNe Ia from the iPTF Survey

SN	MJD	Magnitude	Filter		
iPTF13s	56324.42	19.194 (0.058)	$R_{\mathrm{P48}}$		
iPTF13s	56324.46	19.216 (0.053)	$R_{\mathrm{P48}}$		
iPTF13s	56324.49	19.189 (0.056)	$R_{\mathrm{P48}}$		
iPTF13s	56327.36	18.468 (0.045)	$R_{\mathrm{P48}}$		
iPTF13s	56327.43	18.457 (0.059)	$R_{\mathrm{P48}}$		
iPTF13s	56327.47	18.449 (0.074)	$R_{\mathrm{P48}}$		

**Note.** Table 2 is published in its entirety in the machine-readable format. A portion is shown here for guidance regarding its form and content.

(This table is available in its entirety in machine-readable form.)

and the transformation from Hodgkin et al. (2009) to calibrate the *Y*-band RATIR data ( $Y = J + 0.50 \times (J - H) + 0.08$ ).

All subtracted optical and near-IR photometry for the SNe Ia in our sample are presented in Table 2 and will be available on the WISeREP archive<sup>18</sup> (Yaron & Gal-Yam 2012).

### 4. Analysis

Some of the SNe presented here have previously been published in separate papers:

- 1. Optical and NIR lightcurves and spectra of iPTF13abc (SN 2013bh) were presented and analyzed in Silverman et al. (2013). It is a near identical twin to the peculiar Ia SN 2000cx.
- 2. UV, optical, and NIR lightcurves and spectra of iPTF13asv (SN 2013cv) were presented in Cao et al. (2016) and there is additional *H*-band photometry in Weyant et al. (2018). SN iPTF13asv shows low expansion velocities and persistent carbon absorption features after the maximum, both of which are commonly seen in super-Chandrasekhar events, although its lightcurve shape and sharp secondary near-IR peak resemble characteristic features of normal SNe Ia.
- 3. Optical lightcurves and high-resolution spectra of iPTF13dge were presented in Ferretti et al. (2016), and NIR lightcurves in Weyant et al. (2018). The lightcurves are compatible with that of a normal SN Ia with little reddening, and no definite time variability could be detected in any absorption feature of iPTF13dge.
- 4. UV, optical, and NIR observations of iPTF13ebh from the CSP-II collaboration were presented in Hsiao et al. (2015). SN iPTF13ebh can be categorized as a "transitional" event, on the fast-declining end of normal SNe Ia,

<sup>18</sup> http://wiserep.weizmann.ac.il

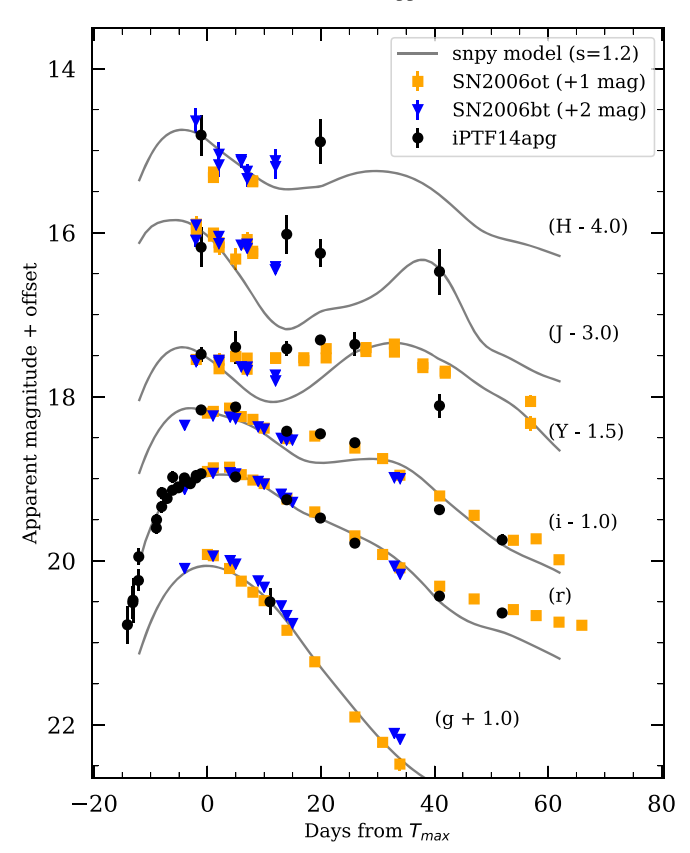


**Figure 4.** Black symbols show our observed lightcurves of iPTF14apg. The SNooPy max\_model fails to accurately fit the lightcurves, shown in gray lines (based on the *r*-band stretch, and offset to match the peak magnitudes). In blue and orange are the lightcurves of peculiar Ia SNe 2006bt and 2006, respectively.

showing NIR spectroscopic properties that are distinct from both the normal and subluminous/91bg-like classes.

- 5. SN iPTF14atg is a subluminous peculiar SN similar to SN 2002es. It displayed strong, declining ultraviolet emission shortly after explosion. Spectra together with UV, optical, and NIR photometry have been extensively analyzed in Cao et al. (2015) and Kromer et al. (2016).
- 6. UV and optical photometry and spectra of the 1999aa-like SN iPTF14bdn were presented in Smitka et al. (2015).
- 7. SN iPTF16abc was analyzed by Miller et al. (2018), Ferretti et al. (2017), and Dhawan et al. (2018b). The rapid, near-linear rise, the unevolving blue colors, and strong absorption from ionized carbon are interpreted to be the result of vigorous mixing of radioactive Ni in the SN ejecta, ejecta interaction with diffuse material, or a combination of the two.
- 8. SN iPTF17lf was a reddened, spectroscopically normal SN Ia, discovered during a wide-area (2000 deg<sup>2</sup>) *g* and *I*-band survey for "cool transients" as part of a two month extension of iPTF (Adams et al. 2018).

For the other SNe included in our sample (except iPTF14ale, which has no spectroscopic classification), we run the Super-Nova IDentification code (SNID Blondin & Tonry 2007) on the spectra (to be presented in a separate paper). For SNe iPTF13s, iPTF13ddg, iPTF13efe, iPTF14bpz, and iPTF14fpb, we rely on redshift estimates based on the SN spectral features using SNID. Furthermore, for iPTF13anh, iPTF13asv, iPTF13azs, iPTF13crp, and iPTF13dkx, we determine the redshifts from narrow host galaxy lines in the SN spectra.

For our single spectrum of iPTF14apg, observed five days before peak brightness, SNID gives a best match to SN 2004dt at  $z=0.088\pm0.004$ , consistent with the spectroscopic redshift of the nearest galaxy. Among the top matches are also SNe 2006ot and 2006bt (Foley et al. 2010), which are peculiar Ia SNe excluded from the Hubble diagram analysis (Burns et al. 2018, Uddin et al. 2020). A direct comparison of the lightcurves of iPTF14apg to those of SNe 2006ot and 2006bt (see Figure 4) strengthens this classification.

### 4.1. Host Galaxies

Figure 5 shows cutout images from the SDSS and PanStarrs surveys, centered on the SN positions. Most SNe can easily be associated with their hosts, while some cases are ambiguous, including:

- 1. SN iPTF14apg: the nearest galaxy is SDSS J123758.69 + 082301.5 with a spectroscopic redshift z = 0.08717, separated by 51", corresponding to a projected distance of 79.4 kpc.
- 2. SN iPTF14bpo: the nearest galaxy is SDSS J171429.74 + 310905.0 with a spectroscopic redshift z = 0.07847, separated by 27", corresponding to a projected distance of 38.9 kpc.
- 3. SN iPTF14ddi: the nearest galaxy is SDSS J171036.45 + 313945.0 with a spectroscopic redshift z = 0.08133, separated by 40", corresponding to a projected distance of 59.2 kpc.

For the literature sample, we note that SNe PTF10hmv, PTF10nlg, and PTF10qyx from Barone-Nugent et al. (2012) have ambiguous hosts.

We estimate the host galaxy stellar mass,  $M_*$ , using the relationship published in Taylor et al. (2011),

$$\log(M_*/M_{\odot}) = 1.15 + 0.7(m_g - m_i) - 0.4M_i.$$
 (3)

We use g- and i-band magnitudes from SDSS (or PanStarrs when no SDSS photometry is available), corrected for the Milky Way (MW) extinction.  $M_i$  is the absolute magnitude in the i band. Table 3 lists the redshifts and coordinates of the SNe in our sample, together with their likely host galaxies and our estimates of the host galaxy stellar mass.

Our mass estimates are consistent with those of Neill et al. (2009), Chang et al. (2015), and Burns et al. (2018), but are systematically higher by  $\sim$ 0.2–0.3 dex than the estimates from Ponder et al. (2020) and Uddin et al. (2020), who employ a more sophisticated spectral energy distribution (SED) fitting (Figure 6). However, for consistency when comparing stellar masses between our sample and the CSP, CfA, and literature sample, we choose to use our estimates for the combined analysis.

### 4.2. Light Curve and Host Galaxy Extinction Fitting

We use the SNooPy lightcurve fitting package developed for the CSP sample (Burns et al. 2011, 2014, 2018) to analyze the lightcurves of the SNe in our sample, including the lightcurves of the literature sample. To find the time of maximum,  $T_{\rm max}$ , the color-stretch parameter,  $s_{BV}$ , and the observed rest-frame peak magnitude of the SNe, the SNooPy max\_model was fitted to the lightcurves. An example fit is shown in the upper panel

 $<sup>\</sup>overline{^{19}}$  The MW extinction is included in the fitted model and the derived magnitudes are corrected for it.

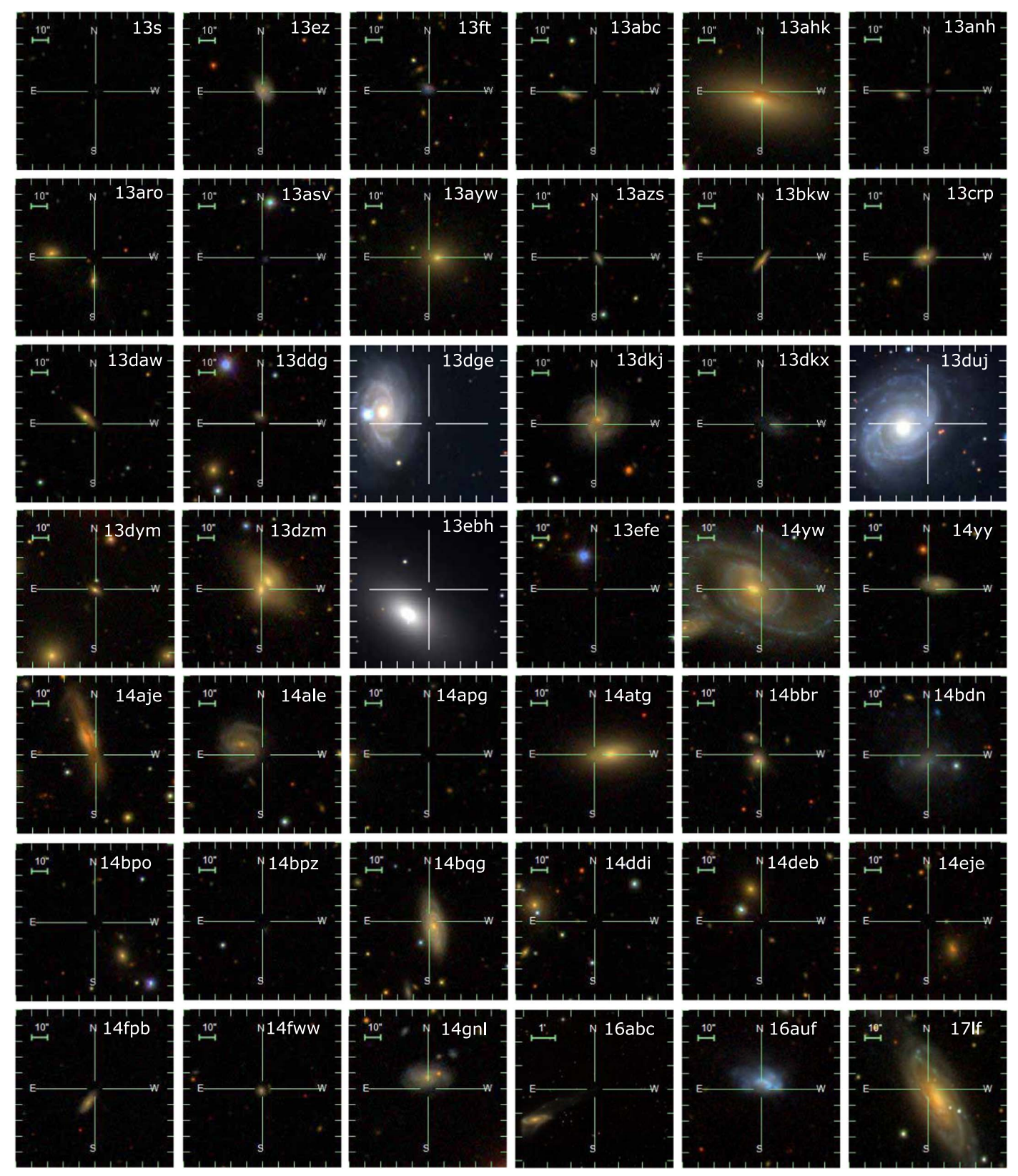


Figure 5. Cutout stamps from SDSS (and PS1) showing the SNe and host galaxies in our sample.

of Figure 7 and the derived lightcurve parameters are given in Tables 4 and 5.

To derive the host galaxy extinction, we use the more elaborated color\_model. This model allows us to fit for the host galaxy extinction taking into account the dependence of

SN Ia intrinsic colors on  $s_{\rm BV}$  (Burns et al. 2014). It uses parameterized dust extinction laws to calculate the total-to-selective extinction ratio  $R_X$  in any filter X as a function of  $R_V$  and  $E(B-V)_{\rm host}$  by the means of synthetic photometry (see Burns et al. 2011). As  $R_V$  controls the wavelength dependence

Table 3
The 42 SNe Ia from the iPTF Survey and Their Associated Host Galaxies

	111	e 42 SNe Ia Irom	the iPTF Survey and	I Their Associated in	ust Galaxies	
SN	$z_{ m helio}$ .	$z_{\rm CMB}$	R.A. (°)	Decl. (°)	Host Galaxy	$\log\left(\frac{M_*}{M_{\odot}}\right)$
iPTF13S	0.059 <sup>a</sup>	0.060	203.222074	+35.959372	SDSS J133253.27 + 355733.4	7.97
iPTF13ez	0.04363	0.04470	182.463737	+19.787693	KUG 1207 + 200	10.19
iPTF13ft	0.03884	0.03963	199.947067	+33.024961	SDSS J131947.32 + 330131.8	8.80
iPTF13abc (SN 2013bh)	0.07436	0.07498	225.554527	+10.645905	SDSS J150214.17 + 103843.6	10.33
iPTF13ahk	0.02639	0.02712	203.805002	+34.678903	NGC 5233	11.27
iPTF13anh	0.0615 <sup>b</sup>	0.0625	196.710215	+15.575657	SDSS J130650.44 + 153432.7	8.51
iPTF13aro	0.08462	0.08497	236.884308	+23.023956	SDSS J154732.26 + 230111.8	10.75
iPTF13asv (SN 2013cv)	0.0362 <sup>b</sup>	0.0364	245.679971	+18.959717	SDSS J162243.02 + 185733.8	7.71
iPTF13ayw	0.05385	0.05418	234.889650	+32.093954	SDSS J153933.08 + 320538.3	11.15
iPTF13azs (SN 2013cx)	0.0338 <sup>b</sup>	0.03376	256.067046	+41.510353	SDSS J170415.96 + 413036.8	9.79
iPTF13bkw	0.06393	0.06491	200.489840	+11.735753	SDSS J132157.57 + 114406.2	10.56
iPTF13crp	0.0630 <sup>b</sup>	0.0621	29.750591	+16.264187	SDSS J015900.28 + 161551.5	10.71
iPTF13daw	0.07755	0.07680	40.880381	+1.984422	SDSS J024331.69 + 015908.4	10.82
iPTF13ddg	0.084 <sup>a</sup>	0.083	11.961798	+31.821517	SDSS J004750.94 + 314922.5	9.71
iPTF13dge	0.015854	0.015805	75.896169	+1.571493	NGC 1762	10.87
iPTF13dkj	0.03623	0.03503	347.211539	+20.069088	CGCG 454-001	10.50
iPTF13dkx	0.0345 <sup>b</sup>	0.0335	20.221425	+3.339925	SDSS J012052.56 + 032023.0	9.13
iPTF13duj (SN 2013fw)	0.016952	0.015879	318.436571	+13.575875	NGC 7042	10.99
iPTF13dym	0.04213	0.04091	351.125804	+14.651100	SDSS J232430.20 + 143903.5	9.93
iPTF13dzm	0.018193	0.017219	17.824325	+33.112441	NGC 0414	10.25
iPTF13ebh	0.013269	0.012493	35.499900	+33.270479	NGC 890	11.23
iPTF13efe	$0.070^{a}$	0.071	130.913761	+16.177023	SDSS J084339.26 + 161037.5	8.39
iPTF14yw (SN 2014aa)	0.016882	0.017972	176.264696	+19.973620	NGC 3861	10.86
iPTF14yy	0.04311	0.04423	186.538205	+9.978942	SDSS J122608.78 + 095847.1	10.40
iPTF14aje	0.02769	0.02825	231.300298	-1.814299	UGC 9839	10.96
iPTF14ale	0.093226	0.093835	219.587725	+27.334341	SDSS J143822.02 + 272010.6	11.36
iPTF14apg	0.08717	0.088278	189.480312	+8.384737	SDSS J123758.69 + 082301.5 (?)	11.01
iPTF14atg	0.02129	0.02222	193.186849	+26.470284	IC 0831	10.88
iPTF14bbr	0.06549	0.06662	186.546284	+7.668036	SDSS J122611.21 + 074000.9	10.85
iPTF14bdn	0.01558	0.016348	202.687002	+32.761788	UGC 8503	8.37
iPTF14bpo	0.07847	0.07838	258.629576	+31.157130	SDSS J171429.74 + 310905.0 (?)	10.77
iPTF14bpz	$0.120^{a}$	0.120	234.215837	+21.767070	SDSS J153651.66 + 214556.5	8.48
iPTF14bqg	0.03291	0.03303	245.986385	+36.228411	SDSS J162356.48 + 361339.3	10.84
iPTF14ddi	0.08133	0.08126	257.639496	+31.659566	SDSS J171036.45 + 313945.0 (?)	11.16
iPTF14deb	0.13243	0.13293	229.614857	+19.742951	SDSS J151828.02 + 194455.3	11.42
iPTF14eje	0.11888	0.11774	348.293114	+29.191366	SDSS J231309.15 + 291111.6	11.38
iPTF14fpb	0.061 <sup>a</sup>	0.060	11.944065	+11.240145	SDSS J004746.83 + 111415.9	10.14
iPTF14fww	0.10296	0.10183	10.326226	+15.438180	SDSS J004118.33 + 152616.2	10.07
iPTF14gnl	0.053727	0.052572	5.951363	-3.857740	SDSS J002348.33 - 035120.6	10.59
iPTF16abc (SN 2016bln)	0.023196	0.024128	203.689542	+13.853974	NGC 5221	10.85
iPTF16auf (SN 2016ccz)	0.01499	0.01563	217.788598	+27.236051	MRK 0685	9.53
iPTF17lf (SN 2017lf)	0.01464	0.01407	48.139952	+39.320608	NGC 1233	10.50

#### Notes.

of the extinction and the host galaxy color excess  $E(B-V)_{\rm host}$  the amount of the extinction, with observations over a broad range of frequencies it is in principle possible to fit independently for  $R_V$  and  $E(B-V)_{\rm host}$ , which are otherwise correlated. In our analysis we use the Cardelli et al. (1989) and O'Donnell (1994) extinction laws. For full details on the color\_model, the reader is referred to Burns et al. (2014, 2018).

We perform two fits for the extinction. First,  $R_V = 2.0$  is assumed for all SN hosts and only  $E(B-V)_{\rm host}$  is fitted. The value  $R_V = 2$  corresponds to our sample average (weighted average  $R_V = 1.9$ ,  $\sigma_{R_V} = 0.8$ ) and is close to values commonly found in many SN Ia cosmological analyses, which commonly employ a single  $R_V$ . Second,

both  $E(B-V)_{\rm host}$  and  $R_V$  are fitted. This is possible because SNe Ia show a small intrinsic color dispersion across the optical to NIR bands and the inclusion of NIR observations provides additional wavelength leverage. Nevertheless, when  $E(B-V)_{\rm host}$  approaches zero (or rather, the level of scatter in the intrinsic color,  $\sigma_{E(B-V)} \sim 0.06$  mag), the leverage to get meaningful constraints on  $R_V$  decreases. The results from the second fit are shown in Table 5. Figure 7 lower panel shows an example of the inferred color excess and the best-fit extinction parameters.

It is a long-standing issue that SN analyses have yielded "unusually"  $^{20}$  low  $R_V$  values. This is seen both when

<sup>&</sup>lt;sup>a</sup> Redshift determined using SNID.

<sup>&</sup>lt;sup>b</sup> Redshift determined from host galaxy lines in the SN spectra.

 $<sup>\</sup>overline{^{20}}$  It may be that the MW average of  $R_V = 3.1$  is unusually high.

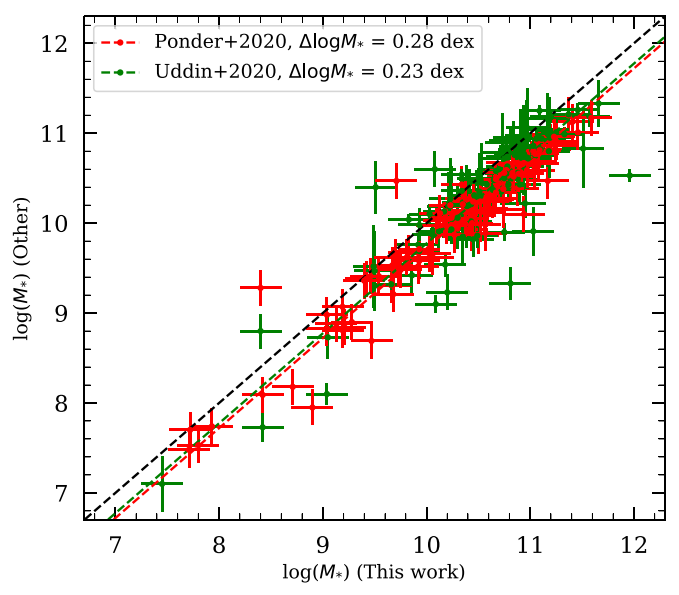


**Figure 6.** Host galaxy mass estimates from this work, compared to those of Ponder et al. (2020) and Uddin et al. (2020) for the SNe in common.

minimizing the Hubble residuals using a global  $R_V$  for cosmological samples and for detailed studies of individual, highly extinguished SNe (e.g., SNe 2006X and 2014J; Amanullah et al. 2014; Burns et al. 2014). We stress that we only use the observed colors to constrain  $E(B-V)_{\rm host}$  and  $R_V$ , since determining extinction by minimizing Hubble residuals can lead to a bias (Burns et al. 2018; Uddin et al. 2020).

### 4.3. NIR Hubble Diagram

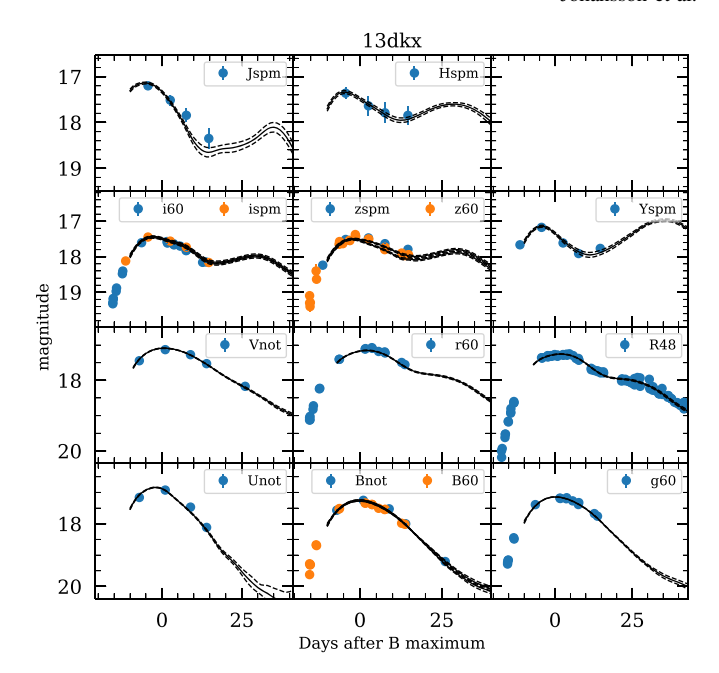
To construct the Hubble diagrams, the distance modulus for filter X,  $\mu_X$ , was computed as:

$$\mu_X = m_X - P_X^N(s_{BV} - 1) - R_{X,BV}E(B - V)_{host},$$
 (4)

where  $P_X^N(s_{BV}-1)$  is the second-order polynomial luminosity decline rate relation from Burns et al. (2018) and  $R_{X,BV}$  is the total-to-selective absorption coefficient for filter X computed from  $R_V$  and  $E(B-V)_{\rm host}$ . Here, we impose that  $R_V>0$  and do not correct for dust extinction objects with  $E(B-V)_{\rm host}<0$ , i.e., intrinsically blue objects.

Figure 8 shows the resulting *J*- and *H*-band Hubble diagrams for our optical+NIR SNe Ia compilation, including 40 SNe from our sample. SNe iPTF14apg and iPTF14atg are not included here, as we do not include spectroscopically peculiar SNe Ia (03fg, 06bt, 02es-like, or Iax SNe) in the analysis. Furthermore we apply a set of cuts on the redshift, stretch, and color excess distribution to our sample, such that we include only SNe with  $z_{\rm CMB} > 0.01$ ,  $s_{BV} > 0.5$ ,  $E(B-V)_{\rm host} < 0.5$  mag, and  $E(B-V)_{\rm MW} < 0.2$  mag (corresponding to typical sample cuts used in other cosmological analyses, e.g., using SALT2 parameters -0.3 < c < 0.3 and  $-3 < x_1 < 3$ ). The solid lines show the best-fit Hubble lines and the dashed lines indicate the scatter expected due to peculiar velocities  $v_{\rm pec} = 300~{\rm km~s}^{-1}$ .

The rms scatter in the Hubble residuals for the combined sample, after the cuts, is  $\sigma_{HR,J} = 0.19$  mag (165 SNe) and  $\sigma_{HR,H} = 0.21$  mag (152 SNe), for J and H, respectively. The scatter in J and H does not decrease significantly when using individual best-fit  $R_V$  instead of a global  $R_V$ .



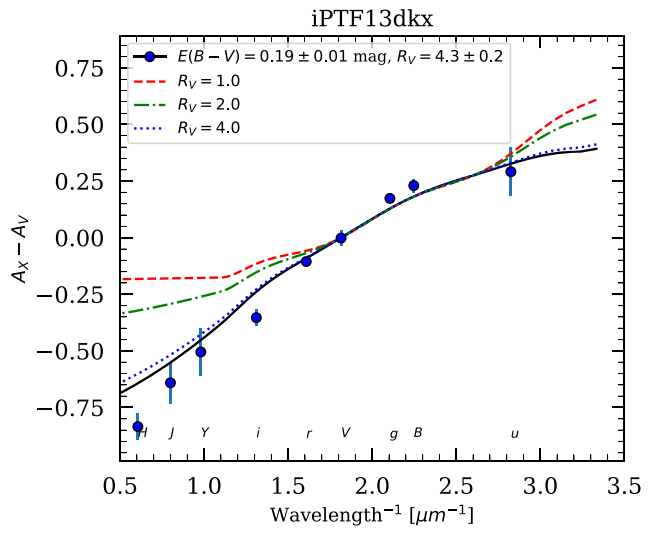


**Figure 7.** Upper panel shows the  $max_model$  fit to iPTF13dkx, a representative SN from our sample at "moderate" redshift and with NIR coverage around peak brightness. Lower panel shows the inferred color excess (normalized with respect to V band) and the best-fit extinction parameters.

We note an offset of  $0.20 \pm 0.05$  mag when comparing the Y-band peak magnitudes to the CSP-I sample (also seen when comparing individual Y-band lightcurves of SNe observed simultaneously by RATIR and CSP-II, C. Burns, private communication). We thus add 0.20 mag to the Y-band magnitudes listed in Table 4 for the Hubble diagram analysis.

### 4.4. Correlations with Host Galaxy Stellar Mass

Having SN host galaxy stellar masses determined in Section 4.1 and color- and stretch-corrected distances from Section 4.3, we can begin to look for correlations.

In Figure 9 we show how our derived color stretch and color excess correlate with host stellar mass. Similar to conclusions reached in previous studies (Sullivan et al. 2011; Childress et al. 2013), we find that low-mass galaxies tend to host SNe with a higher stretch ( $s_{BV} > 0.8$ ) and moderate extinction

 Table 4

 Fitted Lightcurve Peak Magnitudes, k-corrected to Rest Frame and Corrected for MW Extinction Using the SNooPy max\_model

SN	$B_{\max}$	$V_{\rm max}$	$u_{\rm max}$	$g_{ m max}$	$r_{\rm max}$	$i_{\max}$	$Y_{\rm max}$	$J_{ m max}$	$H_{\rm max}$
13 s	•••	•••		17.47 (0.01)	17.75 (0.01)	18.40 (0.06)	18.58 (0.07)	18.22 (0.11)	
13ez		•••	•••	•••	17.43 (0.01)	17.80 (0.06)	17.62 (0.06)	17.72 (0.08)	
13ft		•••	•••	•••	16.84 (0.01)	17.50 (0.02)	17.66 (0.05)	17.46 (0.08)	17.58 (0.13)
13abc	18.29 (0.12)	18.32 (0.09)		18.28 (0.06)	18.27 (0.03)	19.03 (0.05)	19.04 (0.11)	•••	
13ahk	21.02 (0.42)	19.53 (0.39)		20.24 (0.13)	18.66 (0.02)	18.46 (0.10)	17.67 (0.14)	17.18 (0.28)	17.91 (0.30)
13anh	18.11 (0.03)	17.97 (0.03)	18.68 (0.05)		18.19 (0.01)	18.64 (0.01)	18.69 (0.05)	18.58 (0.22)	
13aro	19.04 (0.05)	18.96 (0.04)	19.35 (0.12)	18.93 (0.06)	19.05 (0.02)	19.47 (0.03)	19.38 (0.14)	19.24 (0.31)	•••
13asv	16.32 (0.02)	16.37 (0.02)	16.39 (0.04)	16.28 (0.02)	16.52 (0.01)	17.23 (0.02)	17.50 (0.04)	17.15 (0.04)	17.32 (0.08)
13ayw	18.20 (0.04)	18.18 (0.05)	•••	18.19 (0.03)	18.01 (0.01)	18.50 (0.01)	18.37 (0.06)	18.44 (0.26)	18.14 (0.19)
13azs	17.93 (0.04)	17.58 (0.04)	18.52 (0.06)	17.75 (0.05)	17.60 (0.01)	17.90 (0.01)	17.66 (0.04)	17.31 (0.05)	17.13 (0.08)
13bkw	18.39 (0.03)	18.25 (0.03)	18.66 (0.07)	18.43 (0.02)	18.29 (0.01)	18.83 (0.06)	18.98 (0.15)	19.16 (0.26)	•••
13crp	18.86 (0.02)	18.40 (0.02)	19.21 (0.06)	18.70 (0.05)	18.38 (0.01)	18.82 (0.02)	18.71 (0.28)	18.26 (0.27)	•••
13daw	19.20 (0.02)	•••	•••	19.12 (0.02)	19.08 (0.01)	19.49 (0.03)	19.14 (0.26)	•••	•••
13ddg	18.79 (0.02)	•••	•••	18.78 (0.01)	18.80 (0.01)	19.36 (0.01)	19.22 (0.07)	19.29 (0.26)	•••
13dge	15.13 (0.01)	15.19 (0.01)	15.64 (0.03)	15.28 (0.00)	15.28 (0.01)	15.86 (0.01)	15.80 (0.04)	15.61 (0.08)	15.81 (0.08)
13dkj	17.06 (0.01)	•••	•••	16.97 (0.01)	17.03 (0.01)	17.53 (0.01)	17.33 (0.05)	17.18 (0.11)	17.59 (0.28)
13dkx	17.22 (0.01)	17.04 (0.02)	17.52 (0.04)	17.12 (0.01)	17.11 (0.01)	17.53 (0.01)	17.52 (0.07)	17.19 (0.06)	17.31 (0.05)
13duj	15.11 (0.01)	15.07 (0.01)	15.51 (0.06)	•••	15.09 (0.02)	15.71 (0.02)	15.85 (0.04)	15.69 (0.05)	15.89 (0.05)
13dym	17.75 (0.02)			17.50 (0.02)	17.49 (0.02)	17.86 (0.05)	17.82 (0.09)	17.78 (0.09)	17.83 (0.14)
13dzm	15.81 (0.02)			15.59 (0.02)	15.54 (0.01)	15.94 (0.03)			
13ebh	15.08 (0.01)	14.93 (0.01)	15.75 (0.01)	14.95 (0.01)	14.91 (0.01)	15.32 (0.01)	15.27 (0.04)	15.01 (0.03)	15.20 (0.05)
13efe	18.32 (0.02)	•••	•••	18.28 (0.02)	18.34 (0.02)	18.99 (0.02)	19.13 (0.09)	18.88 (0.33)	•••
14yw		•••	•••	16.08 (0.05)	15.85 (0.02)	16.43 (0.03)	16.43 (0.12)	16.28 (0.14)	•••
14yy	18.43 (0.03)	18.12 (0.05)			18.12 (0.01)	18.50 (0.01)	18.25 (0.03)		
14aje	18.88 (0.06)	18.05 (0.03)	19.67 (0.03)	18.71 (0.02)	17.73 (0.01)	17.75 (0.02)	17.33 (0.08)	16.76 (0.26)	16.85 (0.38)
14ale	19.35 (0.02)			19.33 (0.02)	19.29 (0.01)	19.77 (0.02)	19.50 (0.05)	19.59 (0.13)	19.89 (0.14)
14bbr	18.09 (0.08)			18.10 (0.05)	18.25 (0.03)	18.75 (0.08)	18.79 (0.36)	18.48 (0.14)	18.79 (0.10)
14bdn	14.78 (0.03)	15.04 (0.03)	14.87 (0.04)	14.92 (0.01)	15.45 (0.01)	15.56 (0.04)	15.20 (0.03)	15.42 (0.05)	
14bpo	18.95 (0.07)	•••	•••	18.93 (0.04)	18.98 (0.03)	19.43 (0.07)	19.21 (0.10)	19.09 (0.27)	•••
14bpz	19.83 (0.02)	•••	•••	19.75 (0.01)	19.79 (0.03)	20.43 (0.07)	20.74 (0.29)	•••	•••
14bqg	18.91 (0.05)	18.30 (0.05)	•••	18.70 (0.11)	17.88 (0.02)	18.07 (0.02)	17.67 (0.07)	16.99 (0.08)	17.23 (0.14)
14ddi	19.01 (0.04)			18.90 (0.02)	18.95 (0.01)	19.50 (0.02)		19.47 (0.05)	19.68 (0.05)
14deb	21.00 (0.06)	20.77 (0.04)			20.57 (0.03)			20.60 (0.06)	20.73 (0.06)
14eje	19.42 (0.01)			19.32 (0.04)	19.54 (0.02)	20.08 (0.08)		19.92 (0.15)	20.10 (0.14)
14fpb	18.14 (0.01)	•••	•••	18.02 (0.00)	18.11 (0.01)	18.78 (0.02)	•••	18.78 (0.16)	18.93 (0.13)
14fww	•••	•••	•••	19.40 (0.01)	19.52 (0.06)	20.06 (0.09)	•••	20.08 (0.15)	19.97 (0.11)
14gnl	17.52 (0.04)	17.58 (0.05)	•••	17.53 (0.01)	17.68 (0.02)	18.02 (0.05)	•••	18.07 (0.09)	18.23 (0.13)
16abc	15.95 (0.04)	15.93 (0.05)	16.07 (0.04)	15.81 (0.01)	15.93 (0.01)	16.49 (0.01)	16.67 (0.03)	16.36 (0.03)	16.60 (0.04)
16auf	15.46 (0.02)	15.47 (0.01)	16.24 (0.12)	15.32 (0.01)	15.33 (0.01)	15.70 (0.01)	15.87 (0.05)	15.48 (0.07)	15.73 (0.08)
17lf	•••	•••		18.79 (0.06)	17.27 (0.06)	17.04 (0.03)	16.73 (0.11)		

 $(E(B-V)_{\text{host}} \lesssim 0.25 \text{ mag})$ , while high-mass galaxies also host highly reddened SNe and fast-declining SNe.

Following Stanishev et al. (2018) and references therein, we fit the probability density function (PDF) of the computed color excesses for the entire sample, using an exponentially modified Gaussian distribution with a mean  $c_0$  and standard deviation  $\sigma_c$  and exponent relaxation parameter  $\tau$ . We find values  $c_0 = 0.02$  mag,  $\sigma_c = 0.06$  mag, and  $\tau = 0.14$ . We interpret the Gaussian component as a residual scatter due to intrinsic color variations.

Previous analyses (e.g., Sullivan et al. 2011; Betoule et al. 2014) typically split the sample at  $M_{\rm split}=10^{10}~M_{\odot}$ , which seems to be an "astrophysically reasonable" choice given the fairly distinct difference between the stretch and color excess distributions below and above  $\log(M_*/M_{\odot})=10.0$ . Other analyses have chosen a "statistically motivated" mass split location, either at the median stellar mass  $(\log(M_*/M_{\odot})\sim10.5)$  of their respective sample or based on some information criterion that maximizes the likelihood (Ponder et al. 2020; Uddin et al. 2020; Thorp et al. 2021). We choose to split our sample at  $M_{\rm split}=10^{10}~M_{\odot}$  as our fiducial case. Despite adding more SNe in low-mass galaxies from

our subsample and, e.g., the Barone-Nugent et al. (2012) subsample, the distribution of host stellar mass for our sample is still skewed toward higher  $\log(M_*/M_{\odot})$ . For the combined sample, the median  $\log(M_*/M_{\odot}) = 10.50$ .

If we look at the observed distribution of best-fit  $R_V$  values (Figure 10), we find a weighted average  $R_V = 2.2$  ( $\sigma_{R_V} = 0.9$ ) for  $\log(M_*/M_\odot) < 10.0$  and  $R_V = 1.7$  ( $\sigma_{R_V} = 0.8$ ) for  $\log(M_*/M_\odot) > 10.0$  host galaxies. The weighted average value of  $R_V$  for the whole sample is  $R_V = 1.9$  ( $\sigma_{R_V} = 0.9$ ).

Here, we are not including  $R_V$  estimates for SNe with color excesses close to the level of the intrinsic color scatter  $E(B-V)_{\rm host} < \sigma_c \sim 0.06$  mag (where we typically find artificially low  $R_V$ , albeit with large error bars) or those for highly extinguished SNe with  $E(B-V)_{\rm host} > 0.5$  mag (which are well fit by  $R_V$  values ranging from 1.1 to 2.7, but the distribution is likely to be observationally biased toward finding SNe with low  $R_V$ ).

In order to test the hypothesis that the distributions of  $R_V$  in the low and high stellar mass bins are statistically compatible with being drawn from the same underlying distribution we

Table 5
Lightcurve Parameters for the Supernovae Using the SNooPy color\_model

iPTF13s         56338.13 (0.19)         1.091 (0.027)         0.011         -0.011 (0.013)           iPTF13ez         56346.87 (0.07)         0.879 (0.020)         0.043         0.309 (0.052)           iPTF13ft         56356.87 (0.18)         1.089 (0.015)         0.015         -0.049 (0.028)           iPTF13abc         56385.78 (1.09)         0.850 (0.029)         0.030         0.018 (0.026)           iPTF13ahk         56396.20 (0.36)         0.508 (0.043)         0.013         1.980 (0.057)           iPTF13anh         56414.59 (0.09)         0.945 (0.006)         0.022         0.161 (0.015)           iPTF13aro         56423.93 (0.20)         0.875 (0.027)         0.044         0.186 (0.019)           iPTF13asv         56429.54 (0.16)         1.098 (0.018)         0.044         -0.030 (0.011)           iPTF13ayw         56431.17 (0.14)         0.756 (0.021)         0.029         0.210 (0.017)           iPTF13azs         56436.78 (0.15)         1.035 (0.019)         0.019         0.466 (0.013)           iPTF13crp         56527.92 (0.21)         1.262 (0.016)         0.050         0.407 (0.020)           iPTF13daw         56543.15 (0.56)         0.718 (0.011)         0.034         0.138 (0.021)	2.0 (-) 1.4 (0.2) 2.0 (-) 2.0 (-) 1.1 (0.2) 2.3 (0.4) 2.0 (0.2) 2.4 (1.2)
$\begin{array}{llllllllllllllllllllllllllllllllllll$	2.0 (-) 2.0 (-) 1.1 (0.2) 2.3 (0.4) 2.0 (0.2)
iPTF13abc         56385.78 (1.09)         0.850 (0.029)         0.030         0.018 (0.026)           iPTF13ahk         56396.20 (0.36)         0.508 (0.043)         0.013         1.980 (0.057)           iPTF13anh         56414.59 (0.09)         0.945 (0.006)         0.022         0.161 (0.015)           iPTF13aro         56423.93 (0.20)         0.875 (0.027)         0.044         0.186 (0.019)           iPTF13asv         56429.54 (0.16)         1.098 (0.018)         0.044         -0.030 (0.011)           iPTF13ayw         56431.17 (0.14)         0.756 (0.021)         0.029         0.210 (0.017)           iPTF13azs         56436.78 (0.15)         1.035 (0.019)         0.019         0.466 (0.013)           iPTF13bkw         56459.11 (0.08)         1.014 (0.016)         0.022         0.282 (0.019)           iPTF13crp         56527.92 (0.21)         1.262 (0.016)         0.050         0.407 (0.020)	2.0 (-) 1.1 (0.2) 2.3 (0.4) 2.0 (0.2)
iPTF13ahk         56396.20 (0.36)         0.508 (0.043)         0.013         1.980 (0.057)           iPTF13anh         56414.59 (0.09)         0.945 (0.006)         0.022         0.161 (0.015)           iPTF13aro         56423.93 (0.20)         0.875 (0.027)         0.044         0.186 (0.019)           iPTF13asv         56429.54 (0.16)         1.098 (0.018)         0.044         -0.030 (0.011)           iPTF13ayw         56431.17 (0.14)         0.756 (0.021)         0.029         0.210 (0.017)           iPTF13azs         56436.78 (0.15)         1.035 (0.019)         0.019         0.466 (0.013)           iPTF13bkw         56459.11 (0.08)         1.014 (0.016)         0.022         0.282 (0.019)           iPTF13crp         56527.92 (0.21)         1.262 (0.016)         0.050         0.407 (0.020)	2.0 (-) 1.1 (0.2) 2.3 (0.4) 2.0 (0.2)
iPTF13anh       56414.59 (0.09)       0.945 (0.006)       0.022       0.161 (0.015)         iPTF13aro       56423.93 (0.20)       0.875 (0.027)       0.044       0.186 (0.019)         iPTF13asv       56429.54 (0.16)       1.098 (0.018)       0.044       -0.030 (0.011)         iPTF13ayw       56431.17 (0.14)       0.756 (0.021)       0.029       0.210 (0.017)         iPTF13azs       56436.78 (0.15)       1.035 (0.019)       0.019       0.466 (0.013)         iPTF13bkw       56459.11 (0.08)       1.014 (0.016)       0.022       0.282 (0.019)         iPTF13crp       56527.92 (0.21)       1.262 (0.016)       0.050       0.407 (0.020)	2.3 (0.4) 2.0 (0.2)
iPTF13aro       56423.93 (0.20)       0.875 (0.027)       0.044       0.186 (0.019)         iPTF13asv       56429.54 (0.16)       1.098 (0.018)       0.044       -0.030 (0.011)         iPTF13ayw       56431.17 (0.14)       0.756 (0.021)       0.029       0.210 (0.017)         iPTF13azs       56436.78 (0.15)       1.035 (0.019)       0.019       0.466 (0.013)         iPTF13bkw       56459.11 (0.08)       1.014 (0.016)       0.022       0.282 (0.019)         iPTF13crp       56527.92 (0.21)       1.262 (0.016)       0.050       0.407 (0.020)	2.0 (0.2)
$ \begin{array}{llllllllllllllllllllllllllllllllllll$	* *
iPTF13ayw       56431.17 (0.14)       0.756 (0.021)       0.029       0.210 (0.017)         iPTF13azs       56436.78 (0.15)       1.035 (0.019)       0.019       0.466 (0.013)         iPTF13bkw       56459.11 (0.08)       1.014 (0.016)       0.022       0.282 (0.019)         iPTF13crp       56527.92 (0.21)       1.262 (0.016)       0.050       0.407 (0.020)	2.4 (1.2)
iPTF13azs 56436.78 (0.15) 1.035 (0.019) 0.019 0.466 (0.013) iPTF13bkw 56459.11 (0.08) 1.014 (0.016) 0.022 0.282 (0.019) iPTF13crp 56527.92 (0.21) 1.262 (0.016) 0.050 0.407 (0.020)	
iPTF13bkw 56459.11 (0.08) 1.014 (0.016) 0.022 0.282 (0.019) iPTF13crp 56527.92 (0.21) 1.262 (0.016) 0.050 0.407 (0.020)	2.0 (0.3)
iPTF13crp 56527.92 (0.21) 1.262 (0.016) 0.050 0.407 (0.020)	3.2 (0.2)
	1.0 (0.1)
iPTF13daw 56543.15 (0.56) 0.718 (0.011) 0.034 0.138 (0.021)	2.5 (0.5)
······ (······)	3.9 (0.3)
iPTF13ddg 56547.89 (0.09) 1.014 (0.010) 0.060 0.143 (0.013)	2.5 (0.1)
iPTF13dge 56556.36 (0.02) 1.023 (0.004) 0.078 0.143 (0.007)	2.4 (0.4)
iPTF13dkj 56560.45 (0.06) 0.929 (0.011) 0.147 0.167 (0.006)	2.5 (0.5)
iPTF13dkx 56565.52 (0.10) 1.202 (0.011) 0.027 0.188 (0.008)	4.3 (0.2)
iPTF13duj 56601.58 (0.11) 1.099 (0.017) 0.067 0.150 (0.012)	1.4 (0.2)
iPTF13dym 56610.27 (0.68) 0.541 (0.042) 0.038 0.021 (0.012)	1.9 (1.5)
iPTF13dzm 56614.32 (0.08) 0.675 (0.014) 0.049 0.205 (0.020)	1.6 (0.1)
iPTF13ebh 56623.24 (0.03) 0.609 (0.005) 0.067 0.069 (0.007)	3.1 (1.0)
iPTF13efe 56641.44 (0.27) 1.193 (0.023) 0.021 0.100 (0.010)	1.7 (0.1)
iPTF14yw 56729.58 (0.16) 0.848 (0.029) 0.026 0.276 (0.019)	1.3 (0.4)
iPTF14yy 56733.27 (0.15) 0.802 (0.020) 0.020 0.305 (0.018)	3.2 (0.2)
iPTF14aje 56758.24 (0.10) 0.650 (0.015) 0.152 0.794 (0.018)	2.5 (0.1)
iPTF14ale 56771.54 (0.26) 0.989 (0.025) 0.015 0.289 (0.019)	1.3 (0.3)
iPTF14bbr 56804.28 (0.91) 1.028 (0.054) 0.021 0.122 (0.009)	2.4 (0.2)
iPTF14bdn 56822.23 (0.09) 1.115 (0.012) 0.010 0.100 (0.006)	3.5 (0.3)
iPTF14bpo 56830.32 (0.67) 0.757 (0.026) 0.034 0.066 (0.029)	2.0 (0.1)
iPTF14bpz 56836.01 (0.22) 1.198 (0.022) 0.046 0.090 (0.018)	2.0 (0.3)
iPTF14bqg 56837.98 (0.25) 0.910 (0.050) 0.013 1.076 (0.035)	1.4 (0.3)
iPTF14ddi 56850.63 (0.10) 0.858 (0.016) 0.032 0.099 (0.023)	1.2 (0.1)
iPTF14deb 56841.45 (0.30) 0.613 (0.034) 0.039 0.222 (0.021)	2.2 (0.4)
iPTF14eje 56901.79 (0.66) 1.084 (0.040) 0.108 0.080 (0.016)	3.0 (1.0)
iPTF14fpb 56928.80 (0.53) 1.086 (0.017) 0.072 0.133 (0.017)	1.5 (0.1)
iPTF14fww 56929.64 (0.64) 1.229 (0.035) 0.063 0.081 (0.012)	3.0 (0.2)
iPTF14gnl 56957.26 (0.11) 0.953 (0.017) 0.027 0.083 (0.025)	1.8 (0.6)
iPTF16abc 57499.01 (0.08) 1.070 (0.010) 0.024 0.105 (0.005)	2.4 (0.2)
iPTF16auf 57537.80 (0.09) 1.189 (0.012) 0.013 0.248 (0.021)	2.9 (0.3)
iPTF17lf 57776.60 (0.95) 0.946 (0.032) 0.134 2.129 (0.088)	1.2 (0.1)

perform a Kolmogorov–Smirnov (K-S) test. The K-S test yields a *p*-value of only 0.015, suggesting that the distributions are significantly different, with more than 95% confidence.

Even though the weighted mean values are statistically consistent with the global mean  $R_V$  value, we stress that the wide, non-Gaussian, probability distributions are different.

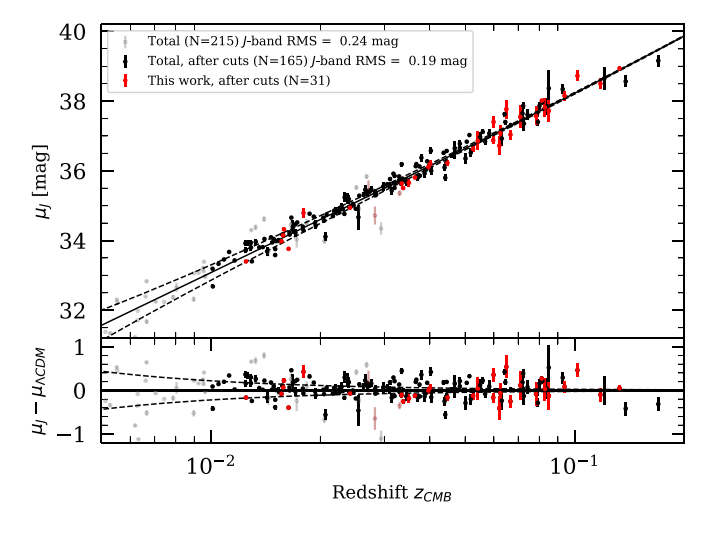
For the low- and high-mass bins, we compute the weighted mean and standard deviation of the Hubble residuals for the BVgriYJH filters (horizontal black lines in Figures 11 and 12). For each filter X, we will refer to any Hubble residual offset between the two bins as a "mass step",  $\Delta_{HR}(X)$ . To further investigate the behavior of the Hubble residuals, we divide the sample into five mass bins (orange symbols in Figure 11), to see if there are any additional effects toward the edges of the host mass distribution. Following Uddin et al. (2020), we also fit a slope to the Hubble residuals as a function of host mass (yellow lines in Figures 11 and 12) using Orthogonal Distance Regression (ODR).

We find that by using a global value  $R_V = 2.0$  (close to the average  $R_V$  for the entire sample) for all SNe in low- and high-

mass host galaxies we reproduce a significant ( $\sim 2\sigma$ ) mass step in optical BVgri-band Hubble residuals  $\Delta_{HR} \sim -0.07 \pm 0.03$  mag, while for NIR JH bands there is no significant mass step ( $\Delta_{HR}(J) = -0.021 \pm 0.033$  mag and  $\Delta_{HR}(H) = 0.020 \pm 0.036$  mag), shown as red symbols in Figure 13 (left panel). A similar trend is seen when fitting a slope to the Hubble residuals as a function of host mass. For optical BVgri-bands we find slopes of  $\sim 0.06 \pm 0.02$  mag dex $^{-1}$ , while in the NIR the slopes are smaller ( $-0.027 \pm 0.016$  mag dex $^{-1}$  and  $-0.005 \pm 0.018$  mag dex $^{-1}$  in J and J, respectively) shown as red symbols in the right panel of Figure 13.

When correcting each SN individually by their best-fit  $R_V \times E(B-V)_{\text{host}}$  we see no significant mass step or mass slope in the Hubble residuals across the optical and NIR bands (blue symbols in Figure 13).

This result seems valid when changing the cuts on z,  $s_{BV}$ , and  $E(B-V)_{\rm host}$ , and perhaps more importantly, the choice of  $M_{\rm split}$ . Choosing  $M_{\rm split}=10^{10.5}\,M_{\odot}$  (the median stellar host galaxy mass of our SNe compilation), we do see a (not significant) mass step across the optical and NIR  $\Delta_{\rm HR}\sim-0.04\pm0.03$  mag. We find



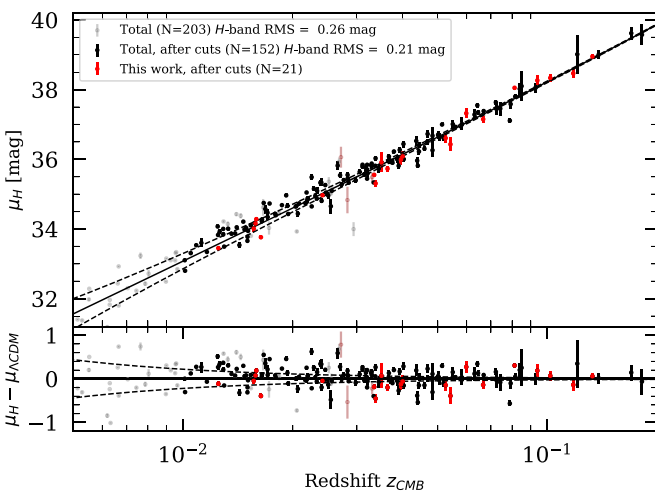


**Figure 8.** *J*- and *H*-band Hubble diagram and Hubble residuals for the SNe surviving our cuts (165 in *J*, 152 in *H*). Red symbols show the SNe presented in this paper, and black symbols the SNe from the literature. Dashed lines indicate the scatter expected due to peculiar velocities  $v_{\text{pec}} \sim \pm 300 \text{ km s}^{-1}$ .

that our results are in line with Brout & Scolnic (2021), who modeled host galaxy reddening as separate Gaussian distributions for galaxies below and above  $\log(M_*/M_\odot) = 10$ . They found that for SNe in low-mass hosts, the average  $\langle R_V \rangle = 2.75 \pm 0.35$ , whereas for SNe in high-mass hosts,  $\langle R_V \rangle = 1.5 \pm 0.25$ , with both subsamples having a wide distribution  $\sigma_{R_V} = 1.3$ . This is in fair agreement with Salim et al. (2018), who found that, on average, dusty, high-mass quiescent galaxies have lower  $R_V$  values ( $\langle R_V \rangle = 2.61$ ), whereas low-mass star-forming galaxies tend to have higher values for  $R_V$  ( $\langle R_V \rangle = 3.15$ ).

Uddin et al. (2020) found nominal evidence for a consistent mass step in both the optical and NIR using the CSP-I sample ( $\Delta_{\rm HR}(J)=-0.103\pm0.050\,{\rm mag}$  and  $\Delta_{\rm HR}(H)=-0.097\pm0.047\,{\rm mag}$ ) using similar cuts on the sample, although including SNe with z<0.01 and having the mass step located at  $\log(M_*/M_\odot)=10.5$  (shown as gray dashed lines in Figure 13). We cannot fully reproduce the NIR mass step reported by Uddin et al. (2020), even if we use their host masses and the same best-fit extinction. We note that they do use updated Phillips relations, correcting for stretch using more flexible spline functions calibrated using unpublished data from CSP-II (C. Burns and S. Uddin, private communication), but we do not expect this to result in the observed differences in our plots.

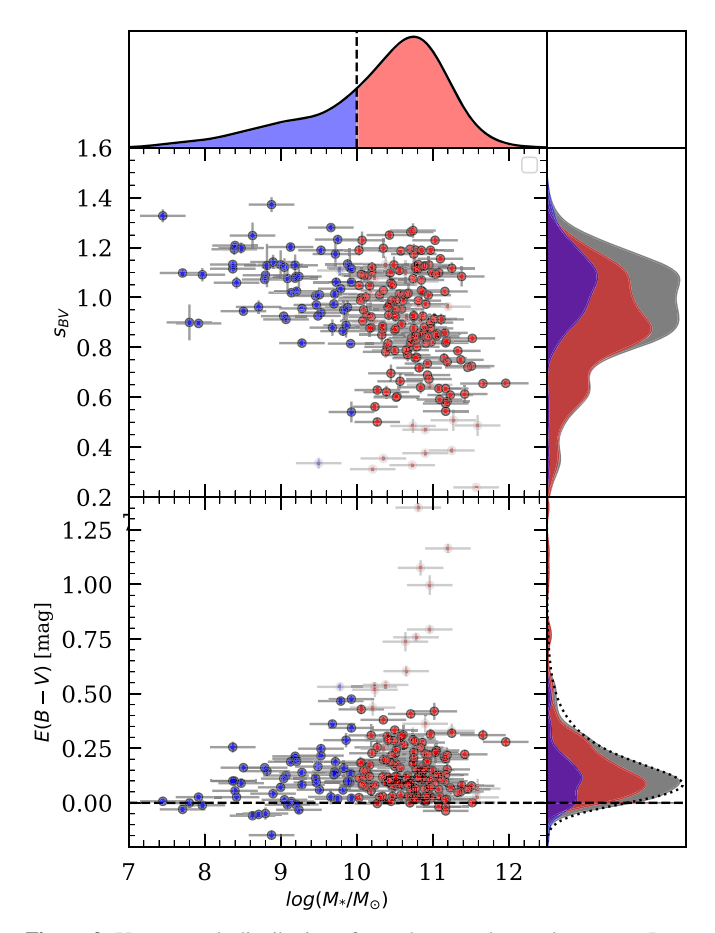


**Figure 9.** Upper panel: distribution of stretch versus host galaxy mass. Low-mass galaxies (blue symbols) preferentially host slow-declining (s > 0.8) SNe, while high-mass galaxies (red symbols) also host fast-declining SNe. Bottom panel: distribution of fitted  $E(B-V)_{\rm host}$  versus host galaxy mass. SNe in low-mass hosts typically have little reddening ( $E(B-V) \lesssim 0.25$  mag.), while there is a tail of highly extincted SNe occurring in high-mass galaxies.

Ponder et al. (2020) also report an H-band mass step  $\Delta_{\rm HR}(H) = -0.18 \pm 0.05$  mag (mass step located at  $\log(M_*/M_\odot) = 10.44$ ) using a compilation of 99 SNe from the literature. However, after removing two outliers, the step reduces to  $\Delta_{\rm HR}(H) = -0.10 \pm 0.04$  mag. For our sample, we find  $\Delta_{\rm HR}(H) = -0.03 \pm 0.04$  mag for a mass step located at  $\log(M_*/M_\odot) = 10.44$ , i.e., consistent with the results from Ponder et al. (2020) in having no NIR mass step. It is unclear if the difference in the results is due to the lack of NIR stretch corrections and/or color corrections, or if it is possibly due to contamination from host galaxy light in unsubtracted photometry from the Sweetspot sample in Weyant et al. (2018).

Recently, Thorp et al. (2021) analyzed optical (*griz*) lightcurves of 157 nearby SNe Ia (0.015 < z < 0.08) from the Foundation DR1 data set using the BayesSN lightcurve fitter (Mandel et al. 2011, 2020). When splitting their sample at  $\log(M_*/M_\odot) = 10.3$ , they find  $\langle R_V \rangle = 2.84 \pm 0.31$  in low-mass hosts and  $\langle R_V \rangle = 2.58 \pm 0.23$  in high-mass hosts (using the Fitzpatrick 1999 extinction law). This is broadly consistent with our results and those of Brout & Scolnic (2021), finding higher  $\langle R_V \rangle$  in low-mass galaxies. However, Thorp et al. (2021) conclude that these values are consistent with the global value of  $\langle R_V \rangle = 2.61 \pm 0.21$ , estimated for the full sample, and cannot be an explanation of the mass step. After corrections, their resulting mass step is marginally reduced,  $\Delta_{\rm HR} = 0.054 \pm 0.025$  mag (shown as the gray dotted line in the left panel of Figure 13).

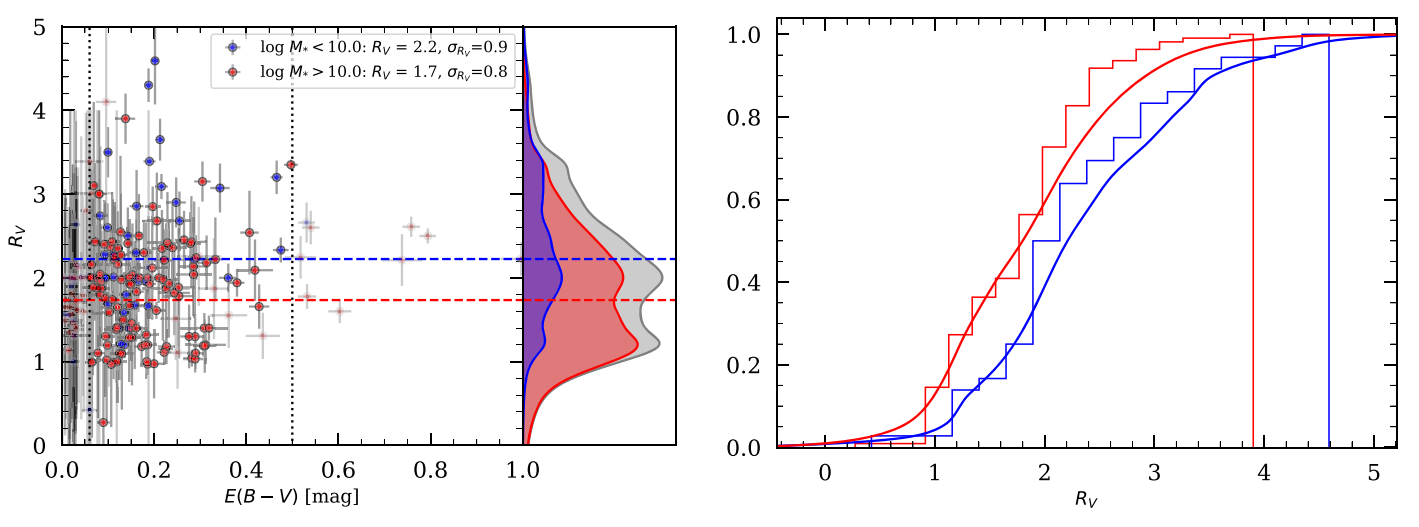


**Figure 10.** Left panel shows the distribution of best-fit  $R_V$  and  $E(B-V)_{\text{host}}$  for the SNe included in the analysis. The color indicates if the SN occurred in a low- (blue) or high-mass host (red). The middle panel shows the coadded probability distribution of the best-fit  $R_V$  values. The right panel shows the cumulative  $R_V$  distribution for the low- and high-mass galaxies in blue and red, respectively.

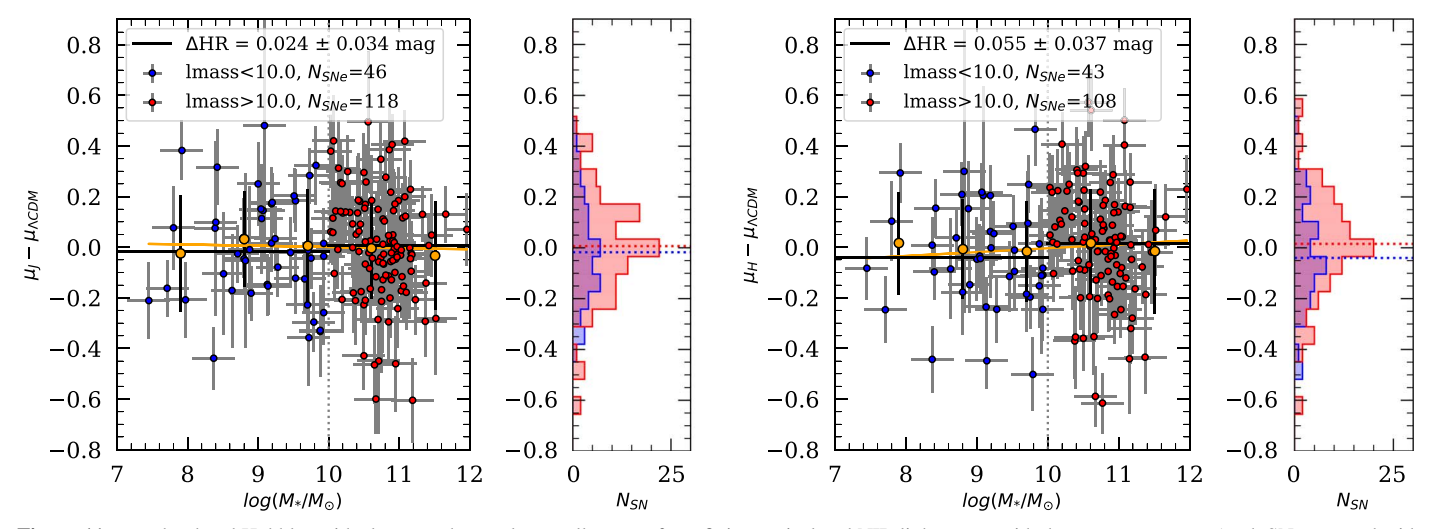


**Figure 11.** *J*- and *H*-band Hubble residuals versus host galaxy stellar mass from fitting optical and NIR lightcurves with the color\_model (each SN corrected with best-fit  $E(B-V)_{\text{host}}$  and  $R_V$ ). Orange symbols show the binned mean and standard deviation of the Hubble residuals in five mass bins, while the orange line is the fitted slope  $(-0.01 \pm 0.02 \text{ mag/dex in } J, 0.0 \pm 0.02 \text{ mag dex}^{-1} \text{ in } H)$ .

#### 5. Discussion

The relation between SN Ia luminosity and host galaxy properties is of great interest for SN Ia progenitor studies as well as for cosmology, as a third empirical correction (Kelly et al. 2010; Lampeitl et al. 2010; Sullivan et al. 2010). While the correlation has been seen nearly ubiquitously across different samples (see, e.g., Brout et al. 2019; Smith et al. 2020), there is a significant debate about the physical origin of this relation. There has been speculation that the mass step may be driven by the age of the stellar population, metallicity, or star formation rate (Sullivan et al. 2010; D'Andrea et al. 2011; Gupta et al. 2011; Hayden et al. 2013; Childress et al. 2014; Rigault et al. 2020; Rose et al. 2021). However, it is possible that this correlation arises due to different SN Ia environments in different host galaxy types.

While most studies pertain to SN luminosity and host galaxy correlations in the optical, recently there have been reports of the possible detection of the mass step in the NIR wavebands (Ponder et al. 2020; Uddin et al. 2020). In this study, we exploit

the multiwavelength, well-sampled lightcurves of the SNe in our sample and compute the mass step/slope after stretch and color corrections, fitting the  $R_V$  parameter individually for each SN. We find that when fitting the  $R_V$  value for each SN, we see a mass step consistent with zero in all filters from B to H band (see Figure 13). However, when fixing the  $R_V$  value to the sample average, as is done in previous studies, we find that there is a mass step of  $\sim 0.07-0.1$  mag in the optical (BVgri), while no significant step is seen in the NIR (YJH).

Since the free  $R_V$  case yields mass steps that are consistent with zero, it is likely that the origin of the mass step is due to variations of dust properties in the interstellar medium of the host galaxies. However, more detailed studies would be required to rule out intrinsic effects. In fact, there are indications that there are two SN populations having different SN ejecta velocities and different intrinsic colors, which also trace the host galaxy stellar mass (see, e.g., Polin et al. 2019; Pan 2020; Siebert et al. 2020). Childress et al. (2013) and Gonzalez-Gaitan et al. (2021) simulate the effect of having separate color—luminosity corrections for low- and high-mass

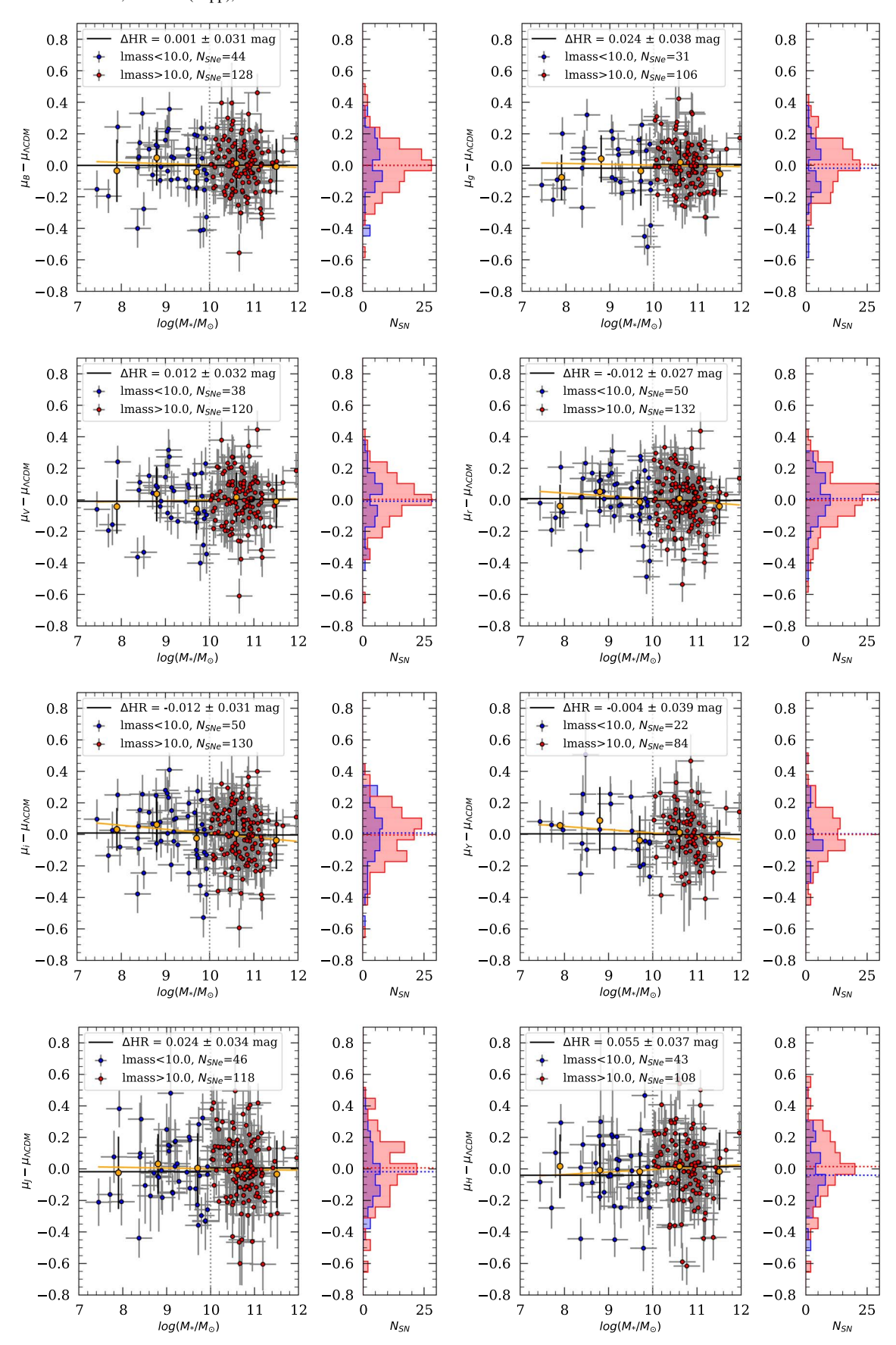


**Figure 12.** Hubble residuals versus host galaxy stellar mass from fitting from optical (BgVri) and NIR (YJH) lightcurves with the SNooPy color\_model (i.e., each SN corrected with best-fit  $E(B-V)_{\text{host}}$  and  $R_V$ ). Orange symbols show the binned mean and standard deviation of the Hubble residuals in five mass bins, while the orange line is the fitted slope.

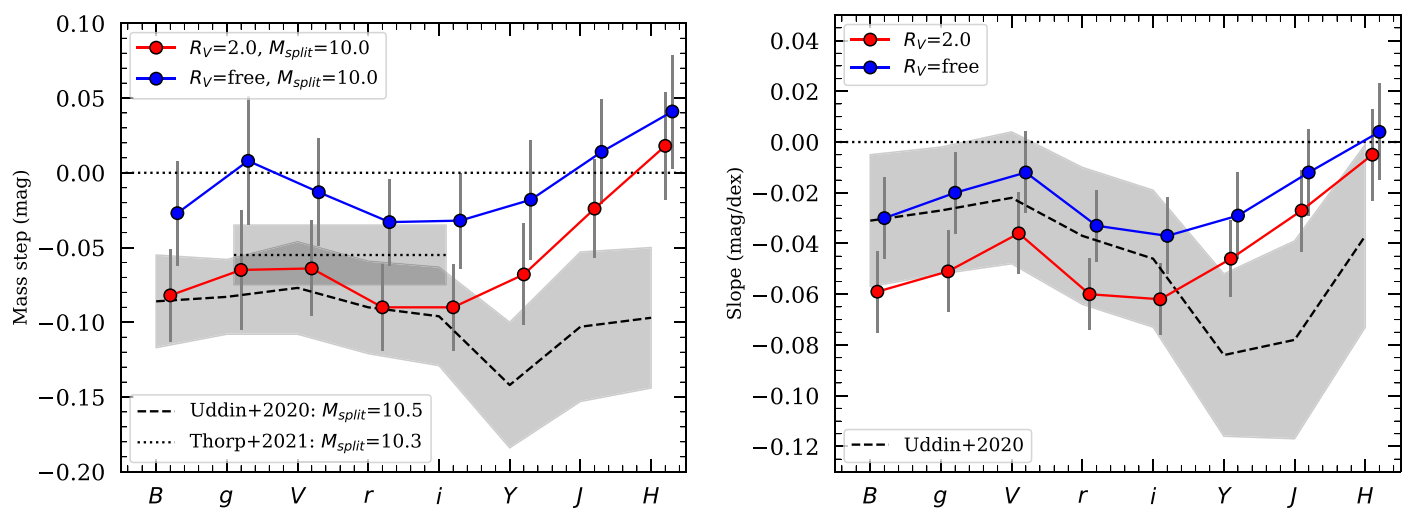


Figure 13. Size of the mass step (left panel) or mass slope (right panel) in different filters (BgVriYJH). Blue symbols show the resulting mass steps/slopes if we use the best-fit  $R_V$  for each individual SN, and red symbols show those for a global  $R_V = 2.0$ . Gray dashed lines show the mass steps from Uddin et al. (2020, their Table 2) for the same cuts on  $E(B - V)_{host} < 0.5$  mag and  $s_{BV} > 0.5$ , but for  $\log M_{split} = 10.5$  and including SNe at z < 0.01. The dotted line shows the mass step in Thorp et al. (2021).

galaxies. They find that multiple free color—luminosity slope parameters may explain away the mass step, suggesting that the origin of the mass step is a difference in the intrinsic color—luminosity relation ( $\beta_{\rm int}c_{\rm int})$  of two SN populations found in galaxies with different masses as opposed to different dust properties.

#### 6. Conclusion

Many studies in the literature have suggested the need for an additional standardization parameter for SNe Ia, beyond the lightcurve shape and color. In particular, firm evidence has been put forward for a correlation between residuals in the Hubble diagram at optical wavelengths and the host galaxy stellar mass (Kelly et al. 2010; Lampeitl et al. 2010; Sullivan et al. 2010; D'Andrea et al. 2011; Gupta et al. 2011; Hayden et al. 2013; Childress et al. 2014; Rose et al. 2021). The underlying cause of these correlations is not completely understood, with some suggestions that this could be due to a correlation with the age/metallicity of the underlying stellar population; however, there is also evidence pointing to this correlation arising from differences in dust properties of the SN hosts

Our work differs from previous studies in that we use a sample of SNe Ia, found in the untargeted PTF/iPTF surveys, that adds a significant number of low-mass host galaxies. Furthermore, our data set includes multiwavelength follow-up observations, including in the near-IR, which allows us to infer the total-to-selective extinction parameter,  $R_V$ , for each SN individually. This is motivated by the findings in, e.g., Amanullah et al. (2015) and Burns et al. (2018), suggesting that the wavelength dependence of dimming by host galaxy mass varies between SNe, making the use of a single value of  $R_V$  questionable. Using a parameterized extinction relation by CCM, we fit for both the color excess, E(B-V), and  $R_V$  using SNooPy color\_model fits of the multiband data. In other words, our estimate of the extinction along the line of sight to each SN is not derived from the Hubble residuals. When examining the Hubble residuals, we do not find a significant correlation with stellar mass at optical or NIR wavelengths.

If we, instead, assume a single value for  $R_V$  to correct all SNe fitting only the color excess, we recover the "mass step" in optical filters. In the NIR, we find no significant dependence on the stellar mass, independent of how  $R_V$  is measured, i.e., individually or globally. This is consistent with the interpretation made by Brout & Scolnic (2021), that the mass step is likely caused by differences in dust properties of the low- and high-mass SN host galaxies.

We are grateful for valuable comments from Jakob Nordin and feedback from the CSP team (Chris Burns, Eric Hsiao, Mark Phillips, and Shuvo Uddin). We thank Melissa L. Graham for helping to obtain follow-up observations with Las Cumbres Observatory in 2013.

A.G. acknowledges support from the Swedish Research Council under Dnr VR 2016-03274 and 2020-03444. T.P. acknowledges the financial support from the Slovenian Research Agency (grants I0-0033, P1-0031, J1-8136 and Z1-1853). Research by S.V. is supported by NSF grants AST-1813176 and AST-2008108.

This work makes use of observations from the Las Cumbres Observatory network. The LCO team was supported by NSF grants AST-1313484 and AST-1911225. The intermediate Palomar Transient Factory project is a scientific collaboration among the California Institute of Technology, Los Alamos National Laboratory, the University of Wisconsin, Milwaukee, the Oskar Klein Center, the Weizmann Institute of Science, the TANGO Program of the University System of Taiwan, and the Kavli Institute for the Physics and Mathematics of the Universe. LANL participation in iPTF is supported by the US Department of Energy as a part of the Laboratory Directed Research and Development program.

Software: FPipe (Fremling et al. 2016), QUBA pipeline (Valenti et al. 2011), lcogtsnpipe (Valenti et al. 2016), IRAF (Tody 1993), astrometry.net (Lang et al. 2010), swarp (Bertin 2010), (Becker 2015), SNooPy (Burns et al. 2011).

### ORCID iDs

- J. Johansson 6 https://orcid.org/0000-0001-5975-290X
- S. B. Cenko https://orcid.org/0000-0003-1673-970X

O. D. Fox https://orcid.org/0000-0003-2238-1572 S. Dhawan https://orcid.org/0000-0002-2376-6979 A. Goobar https://orcid.org/0000-0002-4163-4996 V. Stanishev https://orcid.org/0000-0002-7626-1181 N. Butler https://orcid.org/0000-0002-9110-6673 U. C. Fremling https://orcid.org/0000-0002-4223-103X M. M. Kasliwal https://orcid.org/0000-0002-5619-4938 P. E. Nugent https://orcid.org/0000-0002-3389-0586 T. Petrushevska https://orcid.org/0000-0003-4743-1679 J. Sollerman https://orcid.org/0000-0003-1546-6615 L. Yan https://orcid.org/0000-0003-1710-9339 J. Burke https://orcid.org/0000-0003-0035-6659 G. Hosseinzadeh https://orcid.org/0000-0002-0832-2974 D. A. Howell https://orcid.org/0000-0003-4253-656X C. McCully https://orcid.org/0000-0001-5807-7893 S. Valenti https://orcid.org/0000-0001-8818-0795

#### References

```
Adams, S. M., Blagorodnova, N., Kasliwal, M. M., et al. 2018, PASP, 130,
  034202
Alard, C., & Lupton, R. H. 1998, ApJ, 503, 325
Amanullah, R., Goobar, A., Johansson, J., et al. 2014, ApJL, 788, L21
Amanullah, R., Johansson, J., Goobar, A., et al. 2015, MNRAS, 453, 3300
Avelino, A., Friedman, A. S., Mandel, K. S., et al. 2019, ApJ, 887, 106
Barone-Nugent, R. L., Lidman, C., Wyithe, J. S. B., et al. 2012, MNRAS,
   425, 1007
Becker, A. 2015, HOTPANTS: High Order Transform of PSF ANd Template
   Subtraction, Astrophysics Source Code Library, ascl:1504.004
Bertin, E. 2010, SWarp: Resampling and Co-adding FITS Images Together,
   Astrophysics Source Code Library, ascl:1010.068
Betoule, M., Kessler, R., Guy, J., et al. 2014, A&A, 568, A22
Blondin, S., Dessart, L., & Hillier, D. J. 2015, MNRAS, 448, 2766
Blondin, S., & Tonry, J. L. 2007, ApJ, 666, 1024
Brout, D., & Scolnic, D. 2021, ApJ, 909, 26
Brout, D., Scolnic, D., Kessler, R., et al. 2019, ApJ, 874, 150
Burns, C. R., Parent, E., Phillips, M. M., et al. 2018, ApJ, 869, 56
Burns, C. R., Stritzinger, M., Phillips, M. M., et al. 2011, AJ, 141, 19
Burns, C. R., Stritzinger, M., Phillips, M. M., et al. 2014, ApJ, 789, 32
Butler, N., Klein, C., Fox, O., et al. 2012, Proc. SPIE, 8446, 844610
Cao, Y., Johansson, J., Nugent, P. E., et al. 2016, ApJ, 823, 147
Cao, Y., Kulkarni, S. R., Howell, D. A., et al. 2015, Natur, 521, 328
Cardelli, J. A., Clayton, G. C., & Mathis, J. S. 1989, ApJ, 345, 245
Cenko, S. B., Fox, D. B., Moon, D.-S., et al. 2006, PASP, 118, 1396
Chang, Y.-Y., van der Wel, A., da Cunha, E., & Rix, H.-W. 2015, ApJS, 219, 8
Childress, M., Aldering, G., Antilogus, P., et al. 2013, ApJ, 770, 108
Childress, M. J., Wolf, C., & Zahid, H. J. 2014, MNRAS, 445, 1898
D'Andrea, C. B., Gupta, R. R., Sako, M., et al. 2011, ApJ, 743, 172
Dhawan, S., Bulla, M., Goobar, A., et al. 2018b, MNRAS, 480, 1445
Dhawan, S., Jha, S. W., & Leibundgut, B. 2018a, A&A, 609, A72
Elias, J. H., Matthews, K., Neugebauer, G., & Persson, S. E. 1985, ApJ,
   296, 379
Ferretti, R., Amanullah, R., Goobar, A., et al. 2016, A&A, 592, A40
Ferretti, R., Amanullah, R., Goobar, A., et al. 2017, A&A, 606, A111
Fitzpatrick, E. L. 1999, PASP, 111, 63
Foley, R. J., Narayan, G., Challis, P. J., et al. 2010, ApJ, 708, 1748
Fox, O. D., Kutyrev, A. S., Rapchun, D. A., et al. 2012, Proc. SPIE, 8453,
Fremling, C., Sollerman, J., Taddia, F., et al. 2016, A&A, 593, A68
Friedman, A. S., Wood-Vasey, W. M., Marion, G. H., et al. 2015, ApJS, 220, 9
Gonzalez-Gaitan, S., de Jaeger, T., Galbany, L., et al. 2021, MNRAS,
   508, 4656
Gupta, R. R., D'Andrea, C. B., Sako, M., et al. 2011, ApJ, 740, 92
Guy, J., Astier, P., Baumont, S., et al. 2007, A&A, 466, 11
Hamuy, M., Phillips, M. M., Maza, J., et al. 1995, AJ, 109, 1
Hayden, B. T., Gupta, R. R., Garnavich, P. M., et al. 2013, ApJ, 764, 191
Hodgkin, S. T., Irwin, M. J., Hewett, P. C., & Warren, S. J. 2009, MNRAS,
  394, 675
Hounsell, R., Scolnic, D., Foley, R. J., et al. 2018, ApJ, 867, 23
Hsiao, E. Y., Burns, C. R., Contreras, C., et al. 2015, A&A, 578, A9
```

```
Hubble HST Proposal
Kasen, D. 2006, ApJ, 649, 939
Kelly, P. L., Hicken, M., Burke, D. L., Mandel, K. S., & Kirshner, R. P. 2010,
    pJ, 715, 743
Kelsey, L., Sullivan, M., Smith, M., et al. 2021, MNRAS, 501, 4861
Kirshner, R. P. 2013, in IAU Symp. 281, Binary Paths to Type Ia Supernovae
  Explosions, ed. R. Di Stefano, M. Orio, & M. Moe, 1
Klein, C. R., Kubánek, P., Butler, N. R., et al. 2012, Proc. SPIE,
  8453, 84532S
Krisciunas, K., Contreras, C., Burns, C. R., et al. 2017, AJ, 154, 211
Krisciunas, K., Phillips, M. M., & Suntzeff, N. B. 2004, ApJL, 602, L81
Kromer, M., Fremling, C., Pakmor, R., et al. 2016, MNRAS, 459, 4428
Laher, R. R., Surace, J., Grillmair, C. J., et al. 2014, PASP, 126, 674
Lampeitl, H., Smith, M., Nichol, R. C., et al. 2010, ApJ, 722, 566
Landolt, A. U. 1992, AJ, 104, 340
Lang, D., Hogg, D. W., Mierle, K., Blanton, M., & Roweis, S. 2010, AJ,
  139, 1782
Magnier, E. A., Schlafly, E. F., Finkbeiner, D. P., et al. 2020, ApJS, 251, 6
Mandel, K. S., Narayan, G., & Kirshner, R. P. 2011, ApJ, 731, 120
Mandel, K. S., Thorp, S., Narayan, G., Friedman, A. S., & Avelino, A. 2020,
  arXiv:2008.07538
Mandel, K. S., Wood-Vasey, W. M., Friedman, A. S., & Kirshner, R. P. 2009,
   ApJ, 704, 629
Meikle, W. P. S. 2000, MNRAS, 314, 782
Miller, A. A., Cao, Y., Piro, A. L., et al. 2018, ApJ, 852, 100
Neill, J. D., Sullivan, M., Howell, D. A., et al. 2009, ApJ, 707, 1449
O'Donnell, J. E. 1994, ApJ, 422, 158
Ofek, E. O., Laher, R., Law, N., et al. 2012, PASP, 124, 62
Pan, Y.-C. 2020, ApJL, 895, L5
Perlmutter, S., Aldering, G., Goldhaber, G., et al. 1999, ApJ, 517, 565
Phillips, M. M. 1993, ApJL, 413, L105
Phillips, M. M., Contreras, C., Hsiao, E. Y., et al. 2019, PASP, 131, 014001
Planck Collaboration, Aghanim, N., Akrami, Y., et al. 2020, A&A, 641, A6
Polin, A., Nugent, P., & Kasen, D. 2019, ApJ, 873, 84
Ponder, K. A., Wood-Vasey, W. M., Weyant, A., et al. 2020, arXiv:2006.
Rau, A., Kulkarni, S. R., Law, N. M., et al. 2009, PASP, 121, 1334
Riess, A. G., Casertano, S., Yuan, W., Macri, L. M., & Scolnic, D. 2019, ApJ,
Riess, A. G., Filippenko, A. V., Challis, P., et al. 1998, AJ, 116, 1009
Rigault, M., Brinnel, V., Aldering, G., et al. 2020, A&A, 644, A176
Rose, B., Rubin, D., Strolger, L., & Garnavich, P. 2021, ApJ, 909, 28
Salim, S., Boquien, M., & Lee, J. C. 2018, ApJ, 859, 11
Scolnic, D. M., Jones, D. O., Rest, A., et al. 2018, ApJ, 859, 101
Siebert, M. R., Foley, R. J., Jones, D. O., & Davis, K. W. 2020, MNRAS,
Silverman, J. M., Nugent, P. E., Gal-Yam, A., et al. 2013, ApJS, 207, 3
Skrutskie, M. F., Cutri, R. M., Stiening, R., et al. 2006, AJ, 131, 1163
Smith, M., Sullivan, M., Wiseman, P., et al. 2020, MNRAS, 494, 4426
Smitka, M. T., Brown, P. J., Suntzeff, N. B., et al. 2015, ApJ, 813, 30
Stanishev, V., Goobar, A., Amanullah, R., et al. 2018, A&A, 615, A45
Sullivan, M., Conley, A., Howell, D. A., et al. 2010, MNRAS, 406, 782
Sullivan, M., Ellis, R. S., Aldering, G., et al. 2003, MNRAS, 340, 1057
Sullivan, M., Guy, J., Conley, A., et al. 2011, ApJ, 737, 102
Taylor, E. N., Hopkins, A. M., Baldry, I. K., et al. 2011, MNRAS, 418, 1587
Thorp, S., Mandel, K. S., Jones, D. O., Ward, S. M., & Narayan, G. 2021,
           , 508, 4310
Tody, D. 1993, in ASP Conf. Ser. 52, Astronomical Data Analysis Software
  and Systems II, ed. R. J. Hanisch, R. J. V. Brissenden, & J. Barnes (San
  Francisco, CA: ASP), 173
Tonry, J. L., Stubbs, C. W., Lykke, K. R., et al. 2012, ApJ, 750, 99
Tripp, R. 1998, A&A, 331, 815
Uddin, S. A., Burns, C. R., Phillips, M. M., et al. 2020, ApJ, 901, 143
Uddin, S. A., Mould, J., & Wang, L. 2017, ApJ, 850, 135
Valenti, S., Fraser, M., Benetti, S., et al. 2011, MNRAS, 416, 3138
Valenti, S., Howell, D. A., Stritzinger, M. D., et al. 2016, MNRAS,
  459, 3939
Watson, A. M., Richer, M. G., Bloom, J. S., et al. 2012, Proc. SPIE, 8444,
Weyant, A., Wood-Vasey, W. M., Joyce, R., et al. 2018, AJ, 155, 201
Wiseman, P., Smith, M., Childress, M., et al. 2020, MNRAS, 495, 4040
Wood-Vasey, W. M., Friedman, A. S., Bloom, J. S., et al. 2008, ApJ, 689, 377
Yaron, O., & Gal-Yam, A. 2012, PASP, 124, 668
```

Jha, S. W., Avelino, A., Burns, C., et al. 2019, Supernovae in the Infrared avec